Active species downstream of an Ar–O_2 surface-wave microwave discharge for biomedicine, surface treatment and nanostructuring

2011 Plasma Sources Sci. Technol. 20 035006

(http://iopscience.iop.org/0963-0252/20/3/035006)

Plasma Sources Sci. Technol. **20** (2011) 035006 (17pp) doi:10.1088/0963-0252/20/3/035006

Active species downstream of an Ar–O_2 surface-wave microwave discharge for biomedicine, surface treatment and nanostructuring

Kinga Kutasi[1], **Vasco Guerra**[2] **and Paulo A Sá**[2,3]

[1] Research Institute for Solid State Physics and Optics, Hungarian Academy of Sciences, POB 49, H-1525 Budapest, Hungary
[2] Instituto de Plasmas e Fusão Nuclear, Instituto Superior Técnico, 1049-001 Lisboa, Portugal
[3] Departamento de Engenharia Física, Faculdade de Engenharia da Universidade do Porto, 4200-465 Porto, Portugal

E-mail: kutasi@sunserv.kfki.hu

Received 8 December 2010, in final form 17 March 2011
Published 14 April 2011
Online at stacks.iop.org/PSST/20/035006

Abstract
Self-consistent theoretical models have been developed in order to investigate the early and remote flowing afterglows of a surface-wave Ar–O_2 microwave discharge generated at 2.45 GHz in a 0.5 cm diameter tube at pressures between 1 and 12 mbar. The early afterglow that occurs downstream of the discharge fills up the tube that connects the discharge region with the large-volume processing reactor, where the late afterglow develops. The models provide the time-dependent density profiles of different species along the afterglow and their 3D spatial distribution in the processing reactor. Systematic calculations are performed for all mixture compositions from pure Ar to pure O_2 at different pressures.

It is shown that the Ar^+, Ar_2^+ and O_2^+ can survive up to 1–10 ms in the early afterglow depending on the mixture composition and pressure. In low O_2 content mixtures the ion densities can increase in the early afterglow, depending on the operating conditions, as a result of Penning ionization involving the Ar(4s) states and forming Ar^+, followed by charge transfer. In pure Ar the UV emitting resonant state atoms remain up to 0.1 ms in the afterglow, but with O_2 addition their lifetime becomes considerably shorter. The oxygen species important for many applications, such as $O(^3P)$ atoms and $O_2(a)$ metastable molecules, survive up to 100 ms, thus are the main components of the late afterglow. It is shown that the O_2 molecules are strongly dissociated in the discharge, dissociation being more efficient in high Ar content mixtures. However, the dissociation degree decreases to a few per cent in the early afterglow in about 10 ms. In the case of $O_2(a)$ molecules, yields above the threshold yield for the iodine laser operation are obtained at 12 mbar for afterglow times of up to 10 ms. In the large-volume reactor it has been found that at low pressure the density of $O(^3P)$ atoms decreases by about one order of magnitude towards the walls, while that of O_2(a) changes about 20%, although with pressure the density decreases become more pronounced. Very similar density distributions are found at different mixture compositions for $O(^3P)$ atoms, while the quasi-homogeneous $O_2(a)$ distribution found in high Ar content mixtures progressively turns into a more inhomogeneous one with O_2 addition.

1. Introduction

$Ar–O_2$ plasmas contain several important species, such as oxygen atoms $O(^3P, ^1D)$, metastable oxygen molecules $O_2(a\,^1\Delta_g, b\,^1\Sigma_g^+)$, ozone, and metastable $Ar(^3P_2, ^3P_0)$ and resonant state $Ar(^3P_1, ^1P_1)$ argon atoms [1–9], which favour the application of $Ar–O_2$ discharges in numerous fields. The chemically active oxygen atoms have been found to play a crucial role in plasma based medical sterilization, e.g. bacteria inactivation [10–19] and removal of biological contaminations from surfaces [20–23], as well as in the synthesis of metal-oxide nanowires [24, 25], oxide films deposition [26, 27], functionalization of polymers [28–34], removal of organic impurities [35], selective etching of composites [33, 36], passivation of metals [37, 38], wool treatment [39] and surface activation [3]. The singlet delta oxygen $O_2(a\,^1\Delta_g)$, being a rather active chemical component due to its low excitation energy 0.98 eV [40], is an important agent in biophysical and biochemical processes [41–44], can effectively damage cancer cells [45, 46], and plays as well an important role in the degradation of synthetic polymers [47], in oxygen–iodine laser excitation [40, 48–54] and in combustion processes [55]. The energetic Ar^+ ion has been shown to be involved in the etching of hydrocarbons, together with the O atoms and O_2 molecules, through the so-called chemical sputtering process [56, 57]. Here, the defects on the surface induced by the ions can react with either O_2 molecules or with O atoms creating volatile compounds, such as CO and CO_2. This chemical sputtering has been observed to be a crucial process in the case of etching bacteria spores leading to sterilization [16, 58], as well as in the removal of biological contaminants such as prions, pyrogens and proteins from surfaces [21, 23]. $Ar–O_2$ plasmas are also characterized by a rather intense VUV radiation due to the resonant state $Ar(^3P_1, ^1P_1)$ atoms. The VUV/UV photons below 275 nm can be important in plasma sterilization processes since they have enough energy to break the bonds of C–C (3.8 eV) or C–H (4.5 eV) in a solid and are known to induce strand breaks in DNA [59]. The role of VUV/UV photons from $Ar–O_2$ plasmas in the bacteria inactivation has been studied by several authors [11, 12, 60–62]. A synergetic effect between VUV/UV radiation and the O atoms [11, 18, 63] and between the UV radiation and heat [64] has been found in the sterilization processes, as well as in the case of etching of polyolefins (hexatriacontane—HTC) [29].

The composition of the plasma required by a given application can be controlled by the discharge conditions and initial gas mixture composition. Further tuning possibilities are provided by the flowing afterglow of the discharge, since the lifetime of the various species in the afterglow is very different. In the case of a flowing surface-wave microwave discharge generated with a surfatron typically in a 5–30 mm diameter tube, the early afterglow can be a plasma jet containing excited species as well as ions, while its late afterglow is free of charged species and can fill up large reactors [65, 66]. Therefore, this discharge configuration is favourable for several and diversified applications.

The axial structure of low-pressure argon surface-wave discharges was investigated in [67–71], an axial description of flowing oxygen surface-wave discharges was performed in [72, 73], whereas the $Ar–O_2$ surface-wave microwave discharge was studied in [74]. The aim of this paper is to extend our previous work [74] in order to determine the species densities in the early afterglow of an $Ar–O_2$ surface-wave microwave discharge, as well as their distribution in a large reactor at different discharge conditions for all mixture compositions ranging from pure Ar to pure O_2.

2. Experimental data on the afterglow species densities

The afterglows of $Ar–O_2$ and O_2 surface-wave microwave discharges have been experimentally investigated by numerous groups [34, 75–80]. One of the most frequently used methods for the determination of O atom density in the $Ar–O_2$ afterglow is NO titration. With NO titration the density of O atoms can be determined at the position of NO mixing, quite frequently at the entrance of a post-discharge reactor. Ricard *et al* [75–77] and Belmonte *et al* [34, 78] have carried out density measurements in the afterglow of discharges generated in a 5 mm diameter tube at 2.45 GHz for selected discharge conditions and mixture compositions, as shown in table 1.

Ricard *et al* [75] have determined the [O] density in the afterglow of a 6 mm diameter discharge tube in $Ar–x\%O_2$ mixtures, with x varying between 1 and 54, at two different gas pressures: 1 and 1.3 mbar. The measured densities were between 2×10^{14} and 1.2×10^{15} cm^{-3}. The uncertainty of the NO titration method was estimated to be ±30%.

Mafra *et al* [34] presented the [O] density and the O_2 dissociation degree $[O]/2[O_2]$ in an $Ar–10\%O_2$ mixture at different pressure values. While the density increased from $\approx1.1\times10^{15}$ cm^{-3} to 2.25×10^{15} cm^{-3} in the 2–12 mbar pressure range, the dissociation degree decreased from ≈14–5%.

The dissociation degree, defined in [77] as $\eta = [O]/2[O_2]_0$, where $[O_2]_0$ is the initial O_2 density without plasma, was obtained from NO titration and is presented as a function of microwave power for two O_2 percentages, 5.7% and 9.2%, at 2 mbar and 1 Slmin^{-1} gas flow rate for an afterglow time of ≈10 ms. The dissociation degree has been found to saturate with power, the maximum values obtained for the two O_2 percentages were ≈45% and ≈65%, respectively.

Recently, two further techniques have been developed for the measurement of O atom density, one spectroscopical diagnostic that is based on the emission spectra of the $O_2(b\,^1\Sigma_g^+, v = 0 \rightarrow X\,^3\Sigma_g^-, v' = 0)$ transition [34], and one probe method that relies on the temperature rise of a catalytic probe due to the atomic recombination on the probe surface [79, 81]. These methods, in contrast to NO titration, allow local density measurements in the post-discharge reactor.

Mozetič *et al* have determined the [O] density and O_2 dissociation degree—defined in this case as $[O]kT/p_{O_2}$, where p_{O_2} is the oxygen partial pressure (before discharge ignition)—in the late afterglow of an $Ar–O_2$ surface-wave microwave discharge as a function of the microwave power at an Ar pressure of 2 mbar with the addition of different O_2 percentages [79, 80]. At 110 W the highest dissociation degree was found

Table 1. Summary of the available density measurements in the afterglow of an Ar–O_2 surface-wave discharge generated in a 5 mm tube at 2.45 GHz.

Mixture	p (mbar)	Q (Slmin^{-1})	P (W)	[t] (ms)	[O] (cm^{-3})	Ref.
Ar–30%O_2	1	0.4	50	≈1	1.1×10^{15}	[75]
Ar–9%O_2	1.3	0.6	50	≈1	1×10^{15}	[75]
Ar–2%O_2	3.5	1.1	60	≈10	7×10^{14}	[76]
Ar–10%O_2	4	1.6	60	≈10	1.5×10^{15}	[76]
Ar–10%O_2	4	1	100	≈10	1.7×10^{15}	[34]
Ar–10%O_2	12	1	100	≈10	2.25×10^{15}	[34]
Ar–1.2%O_2	15	1.07	130	≈10	$(2.1 \pm 0.4) \times 10^{14}$	[78]

in Ar–3.9%O_2 ($p_{O_2} = 0.025$ mbar), 80%, while at 160 W the dissociation degree peaked at 75% in Ar–5.7%O_2 ($p_{O_2} = 0.067$ mbar).

Probe measurements have also been conducted in pure O_2 afterglows by Canal *et al* [39] in a reactor used for wool treatment. The O atoms densities obtained at 300 W microwave power were 1.2×10^{15} cm^{-3} and 2.8×10^{15} cm^{-3} at 0.2 mbar and 0.5 mbar, respectively. Still in pure O_2, the O atom density was measured using VUV absorption spectroscopy by Granier *et al* [82] downstream of a surface-wave discharge generated with 390 MHz in a 16 mm diameter tube. Here the decay of the [O] along the flowing afterglow has been monitored at different pressures. At the discharge exit, the dissociation rate, defined in [82] as [O]/2[O_2], has been found to be in the range 2 to 5% for $40 < P < 160$ W and $0.5 < p < 2$ Torr.

3. Post-discharge system configuration

The post-discharge system based on a flowing surface-wave microwave discharge usually consists of a quartz discharge tube, which is connected to a processing reactor (post-discharge reactor) through a Pyrex tube where the early afterglow develops, of diameter comparable to that of the discharge tube [11, 12, 34, 76], as shown in figure 1. The surface-wave discharge is generated with a microwave field typically of frequency $f = 915$ MHz or 2.45 GHz in a tube of inner diameter D that satisfies the $fD \leqslant 4$ GHz cm criterion to obtain a monomode plasma system (the propagation of microwaves is limited to the $m = 0$ mode) [83].

The system investigated here is similar to that of Mafra *et al* [34] in what concerns the discharge and early-afterglow region. In particular, the discharge is generated in a quartz tube of 0.5 cm inner diameter with 2.45 GHz frequency and the discharge tube is connected to the reactor with a Pyrex tube of 2.8 cm inner diameter. For the post-discharge reactor we consider a parallelepipedic reactor made of aluminum, with dimensions of 60 cm × 30 cm × 28 cm similar to the one used by the Montréal group in plasma sterilization experiments [65, 66]. The reactor has one gas inlet of size 2.8 cm × 2.8 cm located in the middle of the left side wall and one outlet on the bottom.

4. Model description

As previously described, the post-discharge system has three main parts: (i) discharge region; (ii) early-afterglow region, which develops downstream from the discharge in the connecting tube between the discharge and the reactor and (iii) late afterglow present in the large volume reactor, also called post-discharge reactor. The species generated in the discharge are carried by the gas flow through the early-afterglow region into the post-discharge reactor. The evolution of the species densities in the different parts of the system can be followed with three different models.

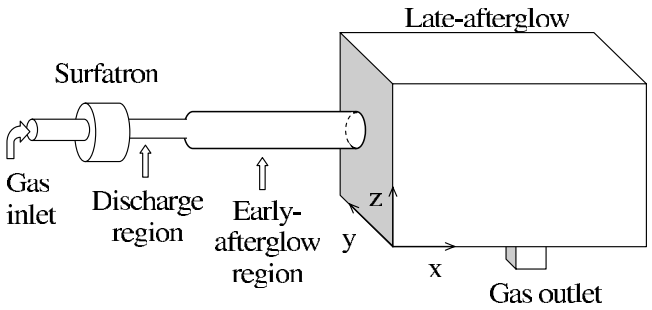

Figure 1. Schematic representation of the basic flowing afterglow system.

The creation of the different species in the discharge is described with a zero dimensional self-consistent kinetic model that is based on the solutions of the electron Boltzmann equation for the microwave field, coupled to a system of rate-balance equations for the neutral and charged heavy species. A detailed description of the model is given in [74], where the gas phase and surface reactions governing the chemical kinetics of the species Ar($^1S_0$, $^3P_2$, $^3P_1$, $^3P_0$, $^1P_1$), $O_2(X\,^3\Sigma_g^-, v)$, $O_2(a\,^1\Delta_g, b\,^1\Sigma_g^+)$, O(^{3}P, ^{1}D), O_3, Ar^+, Ar_2^+, O_2^+, O^+ and O^- are also listed. Since we are interested only in the flowing afterglow of the discharge, the calculations need to be conducted only for the value of the critical electron density, corresponding to the end of the plasma column and determining the density of species leaving the discharge zone. The critical electron density is determined by the condition of the surface-wave mode propagation in a homogeneous, cold, collisionless plasma, surrounded by a dielectric of permittivity ϵ_g, namely $\omega_{pe} > \omega\sqrt{1+\epsilon_g}$, with ω_{pe} and ω denoting the electron plasma angular frequency and the field frequency, respectively. For surface-wave discharges generated at 2.45 GHz in glass tubes ($\epsilon_g = 4$) this electron density is 3.74×10^{11} cm^{-3}.

The evolution of the species along the early-afterglow downstream from the discharge is followed with a system of time-dependent rate-balance equations for the different

Table 2. The viscosity, the thermal conductivity and the specific heat as taken from [27, 89–93]. The temperature T is in K and the pressure p in Pa.

$\mu(\mathrm{Ar}) = 1.57 \times 10^{-5} + 3.81 \times 10^{-8} T$ Pa s
$\mu(\mathrm{O_2}) = (2.72754 + 0.064\,69T - 1.86515 \times 10^{-5} T^2) \times 10^{-6}$ Pa s
$\lambda(\mathrm{Ar}) = 7.31 \times 10^{-3} + 3.71 \times 10^{-5} T$ W m^{-1} K^{-1}
$\lambda(\mathrm{O_2}) = (1.05602 + 0.08791T - 8.91227 \times 10^{-6} T^2) \times 10^{-3}$ W m^{-1} K^{-1}
$\mathrm{C_p(Ar)} = 20.79$ J mol^{-1} K^{-1}
$\mathrm{C_p(O_2)} = 28.168 + \dfrac{6456.6}{788.30\sqrt{\pi/2}} \exp\left(-2\left(\dfrac{T - 1006.9}{788.30}\right)^2\right)$ J mol^{-1} K^{-1}

species. Here, the same chemical-kinetics scheme is used as in the discharge region. However, due to the very low electron energies, the electron impact excitation/ionization processes are omitted. A smooth transition from the ambipolar to free diffusion regimes in the afterglow has been taken into account, as considered in [84, 85]. The effective diffusion coefficient for the electrons and for each of the ionic species is calculated from

$$D_s = D_\mathrm{a} \frac{D_\mathrm{f} + \Lambda^2 e n_\mathrm{e} \mu_\mathrm{e} / \epsilon_0}{D_\mathrm{a} + \Lambda^2 e n_\mathrm{e} \mu_\mathrm{e} / \epsilon_0}, \tag{1}$$

where, for each species, D_a is the ambipolar diffusion coefficient, calculated for the end of discharge conditions [86], D_f is the free diffusion coefficient, $\Lambda = R/2.405$ is the characteristic diffusion length for a cylindrical container of radius R, e is the electron charge, μ_e the electron mobility and ϵ_0 the vacuum permittivity. Clearly this is only an approximation, as the expression is derived for electrons and in the discharge, but it allows us to have an estimation of the lifetime of ions and electrons in the flowing afterglow. The presence of charged particles in the afterglow can be desirable or undesirable, depending on the applications. The species densities are thus obtained in the early afterglow as a function of the afterglow time (the flight-time of the species in the afterglow), which can be transformed into afterglow position by knowing the gas pressure, tube radius and gas flow rate. These time-dependent densities allow us to determine the density of species at the entrance of the post-discharge reactor.

In the post-discharge reactor the density distributions of the various species are determined with the help of a three-dimensional hydrodynamic model, comprising (i) the total mass conservation equation (2), (ii) the continuity equations for the different species equation (3), (iii) the total momentum conservation equation (4) and (iv) the total energy conservation equation (5):

$$\int_S \rho \boldsymbol{v} \cdot \boldsymbol{n} \mathrm{d}S = 0, \tag{2}$$

$$\int_S \rho y_k \boldsymbol{v} \cdot \boldsymbol{n} \mathrm{d}S - \int_S \mathrm{grad}\,(D_k \rho y_k) \cdot \boldsymbol{n} \mathrm{d}S = \int_V m_k S_k^\mathrm{V} \mathrm{d}V + \int_S m_k S_k^\mathrm{S} \mathrm{d}S, \tag{3}$$

$$\int_S \rho u_i \boldsymbol{v} \cdot \boldsymbol{n} \mathrm{d}S = \int_S \mu\, \mathrm{grad}\, u_i \cdot \boldsymbol{n} \mathrm{d}S - \int_S p \boldsymbol{i}_i \cdot \boldsymbol{n} \mathrm{d}S, \tag{4}$$

$$\int_S \rho T \boldsymbol{v} \cdot \boldsymbol{n} \mathrm{d}S = \int_S \frac{\lambda}{C_p}\, \mathrm{grad}\, T \cdot \boldsymbol{n} \mathrm{d}S. \tag{5}$$

Here ρ denotes the total gas density, $\boldsymbol{v}$ the gas velocity and $\boldsymbol{n}$ the unit vector orthogonal to the S surface and directed outwards. Further, y_k denotes the relative mass density ($y_k = \rho_k/\rho$), D_k and m_k are the diffusion coefficient and the mass of the species k, respectively, and S_k^V and S_k^S represent the source terms associated with volume and surface reactions, respectively. Since S_k^S represents the surface losses, it is considered in (3) only on the last grid point at the proximity of the surface. u_i is the velocity in the i direction, p the static pressure, μ the dynamic viscosity, T the gas temperature, C_p the specific heat at constant pressure and λ the thermal conductivity. A more detailed description of the model is given in [87, 88]. The transport data used in the model is presented in table 2. In what concerns the molecular kinetics, the same chemical-kinetics scheme is used as in the discharge. However, due to the recombination of charged species along the early afterglow region, here we neglect the electrons and ions.

One important parameter that changes from region to region is the surface recombination probability of atoms, because of the surface temperature gradient along the system and of the use of different wall materials. Wall temperatures as high as ~400 K are reached in the discharge region, in the early afterglow they decrease to ≈330 K, while in the post-discharge reactor the wall is at room temperature ≈300 K. Furthermore, the discharge and early afterglow tubes are made of Quartz and Pyrex, respectively, while the post-discharge reactor is of aluminum. The temperature dependent recombination probability of O atoms (γ) measured by Macko *et al* [94] for a Pyrex surface exposed to an oxygen dc discharge shows a sharp increase with the temperature above 300 K, reaching values as high as 2×10^{-2} at 500 K. In accordance with these measurements for the discharge region we chose $\gamma_{\mathrm{O}(^3\mathrm{P})} = 8 \times 10^{-3}$, while for the early afterglow region we take $\gamma_{\mathrm{O}(^3\mathrm{P})} = 4 \times 10^{-3}$. In the case of the late-afterglow present in the aluminum reactor, we use the data of Mozetič [95], $\gamma_{\mathrm{O}(^3\mathrm{P})} = 2 \times 10^{-2}$, determined in a pure O_2 flowing afterglow at 0.5 mbar and $T_\mathrm{s} = 300$ K. For $O_2(a)$ molecules we take $\gamma_{\mathrm{O_2(a)}} = 5 \times 10^{-4}$ in accordance with the results of Sharpless *et al* [96], while $\gamma_{\mathrm{O_2(b)}} = 2 \times 10^{-2}$ [97].

Another critical input parameter of the model is the gas temperature. However, its value is not available for different discharge conditions. Although the temperature depends on the pressure and the O_2 addition to Ar, due to the lack of data we use for all conditions a discharge temperature $T_\mathrm{g} = 500$ K and in the early afterglow 350 K, in compliance with the measurements of Belmonte *et al* [98], who found $T_\mathrm{g} = 450$ K at 4.4 mbar in Ar–10%O_2.

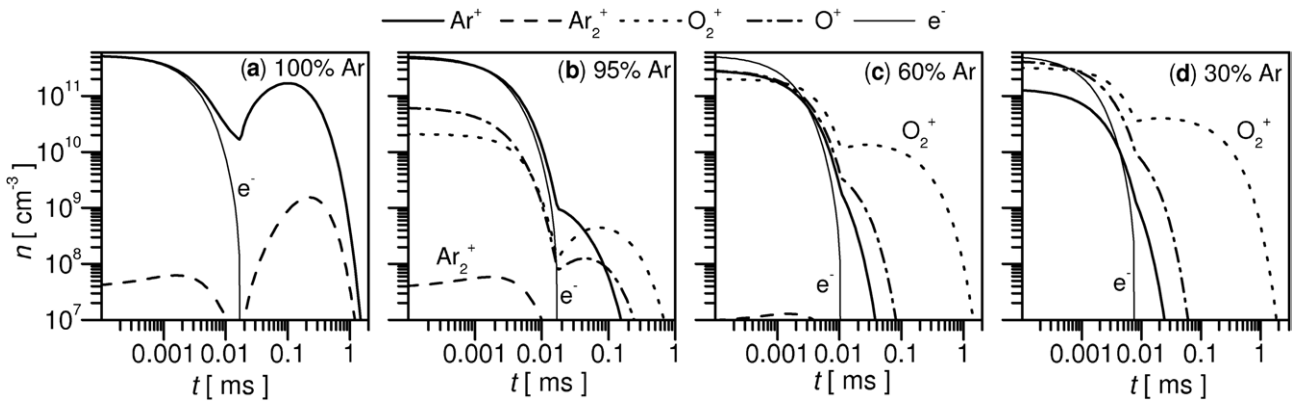

Figure 2. Positive ions and electron densities along the early afterglow as a function of the afterglow time, at 1 mbar, for different mixture compositions.

5. Results and discussion

The experimental investigations available in the literature, as presented in section 2, have been conducted mostly in mixtures with low O_2 content ($\leqslant$10%) at selected pressure values in the 1–15 mbar range either in the early or late-afterglow regions. In order to have a more complete picture of the system we have conducted systematic calculations by covering the full mixture range from pure Ar to pure O_2, for pressures in the interval 1–12 mbar for both the early afterglow and late-afterglow regions.

The compositions of the plasma calculated in the early and late afterglow are presented in two different sections. For the early afterglow region the species densities are presented as a function of the flight-time along this region, which can be transformed into spatial distributions by knowing the applied gas flow rate. Note that since a given flight-time can be achieved with different gas flow rates—tube length combination, these time-dependent results are more general than the spatial distributions. In the case of the late afterglow, we present the spatial distribution of the species concentrations in the processing reactor described in section 3.

5.1. Early afterglow

5.1.1. Positive ions. As suggested by the experimental investigations, a number of applications, such as the biological decontamination of surfaces [21, 23], nanostructure deposition [25] and surface treatments [29–31, 35, 37], may call for the presence of ions. The calculations conducted for the discharge region (end of the plasma column at critical electron density for the surface-wave propagation) have shown that the charge composition of the plasma depends on the initial gas mixture composition, as well as on the gas pressure (figure 8 in [74]). Regarding the afterglow, the most important information is how long the different species can survive. Therefore, in this section we discuss the lifetime of several charged species, for different initial discharge mixture compositions and gas pressure values.

Figures 2(*a*)–(*d*) show the densities of various charged species as a function of the afterglow flight-time, at 1 mbar and for different initial mixture compositions. In the case of pure Ar, figure 2(*a*), the dominant ions are Ar^+, as expected, which at this pressure can survive up to ~1 ms. The electrons are lost in the afterglow at about 0.01 ms, which favours the longer survival of ions, helped also by the creation through the metastable–metastable ionization process (often denoted by pooling or Penning ionization), $Ar(4s_j) + Ar(4s_i) \rightarrow Ar(^1S_0) + Ar^+ + e$. Indeed, the decrease in electron–ion recombination losses and the dominance of Penning ionization is marked by an increase in the concentrations of the positive ions, taking place after 0.01 ms. At the maximum densities in the afterglow, the difference between the populations of the atomic and molecular argon ions is about two orders of magnitude. The density of these two ionic species is correlated through the $Ar^+ + Ar(^1S_0) + Ar(^1S_0) \rightarrow Ar_2^+ + Ar(^1S_0)$ associative charge transfer process. A small addition of O_2 to Ar, such as 5%, changes considerably the charge composition of the afterglow plasma, as illustrated in figure 2(*b*). After the electron disappearance, O_2^+ becomes the dominant ionic species. The concentrations of O_2^+ and O^+ pass through a maximum in the afterglow, similar to the one calculated for Ar^+ and Ar_2^+ in pure argon, which is due to the charge transfer mechanisms $O(^3P) + Ar^+ \rightarrow Ar(^1S_0) + O^+$ and $O_2 + Ar^+ \rightarrow Ar(^1S_0) + O_2^+$, helped by the creation of Ar^+ ions by Penning ionization. The effect is less pronounced than in pure argon, as the O atoms and O_2 molecules also quench the Ar metastables, which contribute to ionization, very efficiently through the $Ar(4s_j)+O_2(X, 0) \rightarrow Ar(^1S_0)+O(^3P)+O(^3P)$, $Ar(4s_j) + O_2(X, 0) \rightarrow Ar(^1S_0) + O(^3P) + O(^1D)$, and $Ar(4s_j) + O \rightarrow Ar(^1S_0) + O$ processes. In this case, Ar^+ and O^+ ions disappear by about 0.1 ms, while the O_2^+ ions survive up to ≈0.4 ms. With further oxygen addition the quenching of the Ar metastables by O and O_2 makes the creation of Ar^+ ions by Penning ionization negligible. The lifetime of the dominant ion, O_2^+, becomes very long as shown in figure 2(*c*) for a 60%Ar–40%O_2 mixture and in figure 2(*d*) for a 30%Ar–70%O_2 mixture. The differences in the charge composition of the afterglow plasma for these two discharge mixtures are minor, although small changes in the lifetimes can be observed.

It is worth noting that electron losses by diffusion are always at least one order of magnitude higher than the losses by electron–ion recombination. For the present conditions, the latter process does not have a significant contribution to the formation of the time-dependent profiles of the charged

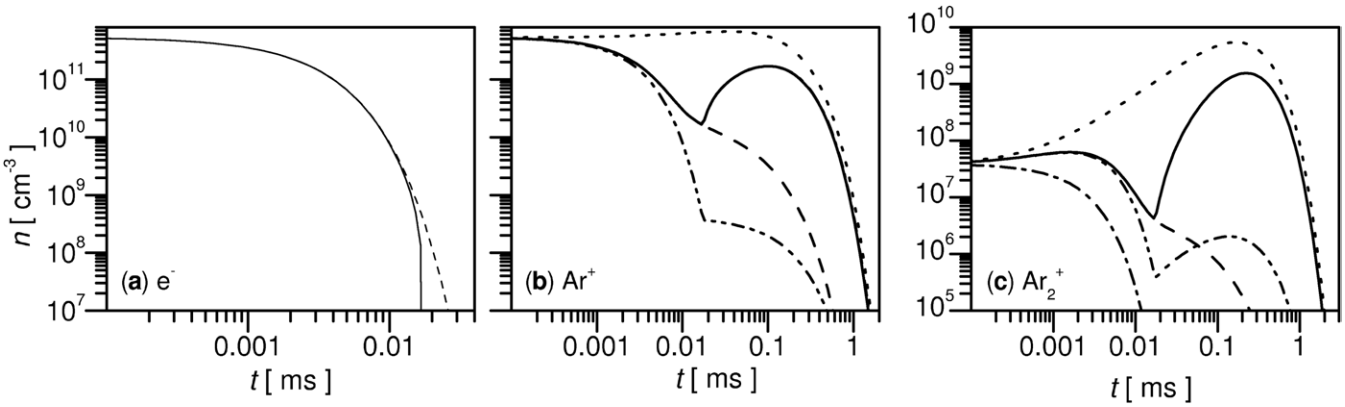

Figure 3. Densities of (*a*) electrons, (*b*) Ar^+ and (*c*) Ar_2^+, considering: the transition from ambipolar to free diffusion regimes in the afterglow (——); ambipolar diffusion only (– – –); free diffusion only (· · · · · ·); eliminating reaction $Ar^+ + Ar(^1S_0) + Ar(^1S_0) \rightarrow Ar_2^+ + Ar(^1S_0)$ (— · —) and eliminating reaction $Ar(4s_j) + Ar(4s_i) \rightarrow Ar(^1S_0) + Ar^+ + e$ (— · · —).

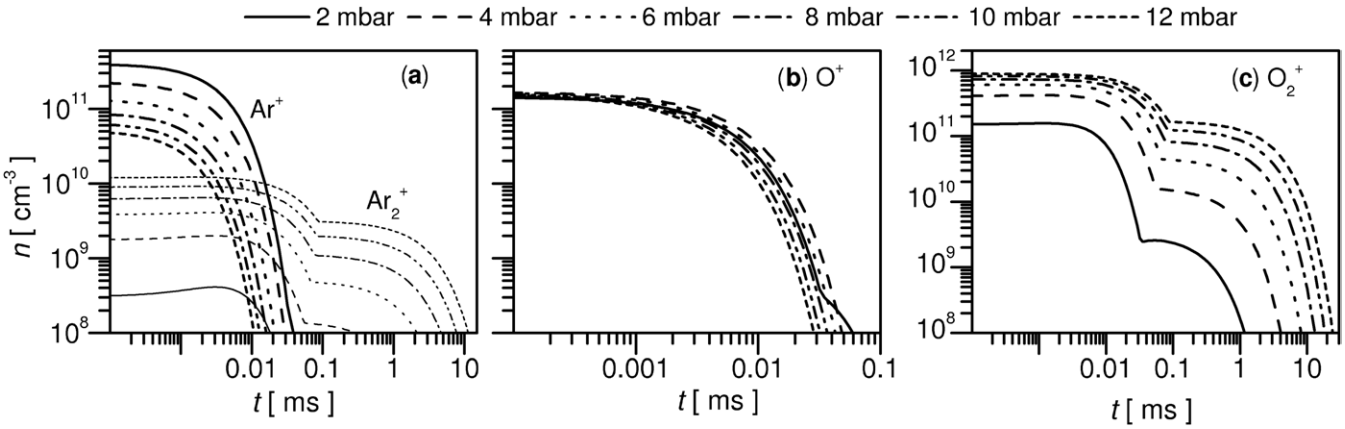

Figure 4. Densities of different positive ions (*a*) Ar^+ and Ar_2^+, (*b*) O^+ and (*c*) O_2^+ for the 90%Ar–10%O_2 mixture at different gas pressures.

species. This was verified by removing the electron–ion recombination processes from the kinetic scheme presented in [74]. For the same conditions as in figure 2, no perceivable difference in the concentrations of electrons and ions was found.

The influence of the transition from the ambipolar to free diffusion regimes in the early afterglow can be evaluated in figure 3, which reveals as well the importance of the Penning ionization and charge transfer processes. As expected, if only free diffusion is considered in the early afterglow, electrons and positive ions disappear much faster and slower, respectively, as compared with the base calculations (note that the curve corresponding to the electron density if free diffusion is assumed to prevail in the early afterglow does not appear in figure 3(*a*), because n_e becomes vanishingly small for times of the order of 10^{-8} s). The reverse is true if ambipolar diffusion is considered all along the afterglow. Therefore, an adequate treatment of diffusion is important if the lifetime of ions and electrons in the afterglow is to be estimated. It is also interesting to quantify the effects of the Penning ionization mechanism $Ar(4s_j) + Ar(4s_i) \rightarrow Ar(^1S_0) + Ar^+ + e$ and of the associative charge transfer reaction $Ar^+ + Ar(^1S_0) + Ar(^1S_0) \rightarrow Ar_2^+ + Ar(^1S_0)$. To this purpose, figure 3 depicts as well the densities of the ionic species when each of the processes is not included in the calculations and the transition from ambipolar to free diffusion is considered. As it can be seen, these two reactions are responsible for the unfamiliar enhancement of the concentrations of Ar^+ and Ar_2^+ ions in the afterglow. A similar effect has been observed experimentally by Kang *et al* in the afterglow of a pulsed ICP discharge, where a peak in the recombination radiation was registered at 0.1 ms afterglow time [99].

In figure 4 we present the pressure dependence of the ion populations in the case of 90%Ar–10%O_2, a mixture that is preferred in several experimental investigations [34, 76]. For the argon ions, we can observe in figure 4(*a*) a faster disappearance of the atomic ions with pressure, while the density of Ar_2^+ increases, as well as their lifetime, which reaches 10 ms at 12 mbar. Regarding O^+, pressure has a minor effect on both its density and lifetime, as seen in figure 4(*b*). As for molecular O_2^+ ions, a considerable increase in density and lifetime is obtained with pressure: at 12 mbar it can survive more than 10 ms. The main loss mechanisms of O_2^+ ions are diffusion to the wall and ion–ion recombination with O^-, the former being more important at the lower pressures. In turn, O_2^+ is created in the afterglow by the charge transfer process involving O^+ and Ar^+.

5.1.2. UV radiation. The UV radiation in the Ar–O_2 system is provided by the Ar resonant states $Ar(^3P_1)$ and $Ar(^1P_1)$, whose densities are strongly correlated with the density

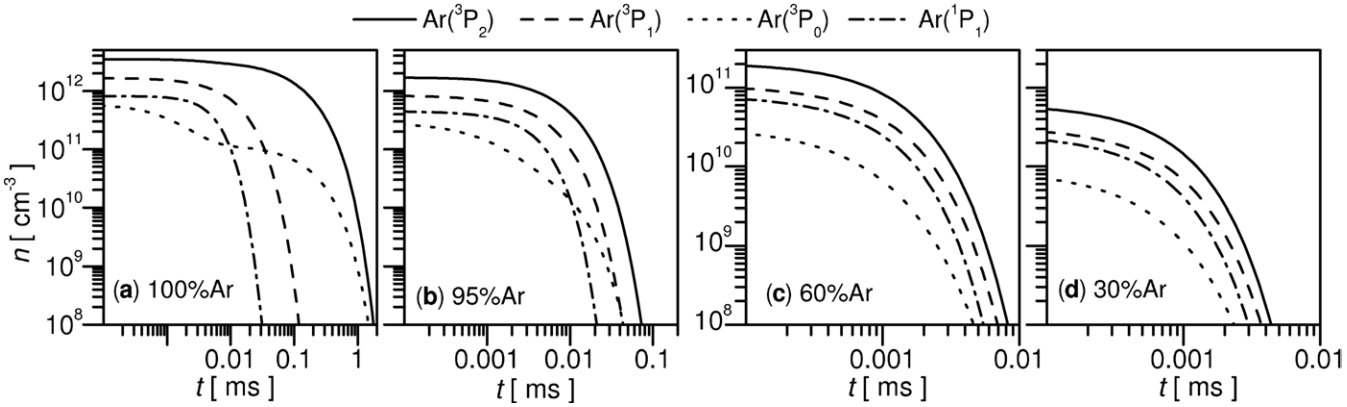

Figure 5. Densities of metastable and resonant state argon atoms along the early afterglow as a function of the afterglow time, at 1 mbar, for different mixture compositions.

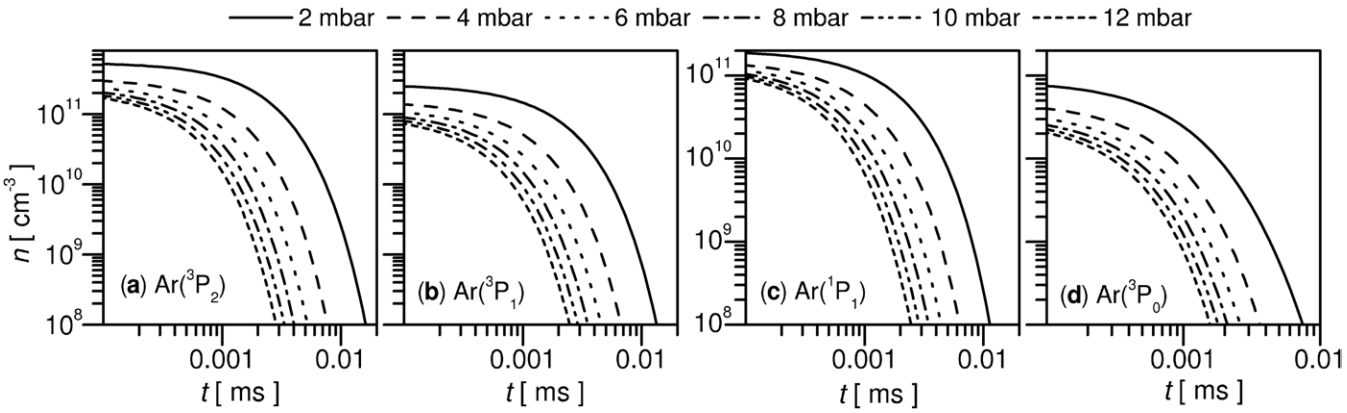

Figure 6. Densities of different Ar atomic states (*a*) $Ar(^3P_0)$, (*b*) $Ar(^3P_1)$, (*c*) $Ar(^1P_1)$ and (*d*) $Ar(^3P_0)$ for the 90%Ar–10%O_2 mixture at different gas pressures.

of metastable atoms $Ar(^3P_0)$ and $Ar(^3P_2)$ [74, 100, 101]. Figures 5(*a*)–(*d*) shows the evolution of the metastable and resonant state atoms in the afterglow for different initial mixture compositions at 1 mbar. In pure argon, figure 5(*a*), the metastable atoms can survive up to 1 ms, while the resonant atoms $Ar(^3P_1)$ and $Ar(^1P_1)$ survive up to 0.1 ms and 0.03 ms, respectively. With the addition of O_2 to Ar the lifetime of metastable and resonant state atoms decreases considerably in the afterglow, due to their quenching by O_2 and O atoms. With 5% of O_2 in the mixture, the metastable and the radiative Ar species disappear in less then 0.1 ms, see figure 5(*b*), while in 60%Ar–40%O_2 their lifetimes are less then 0.01 ms, figure 5(*c*).

Figures 6(*a*)–(*d*) present the density of metastable and resonant state atoms along the afterglow at different pressures in the 90%Ar–10%O_2 mixture. Here, the lifetimes of both radiative and non-radiative atoms are typically a few times 0.001 ms in the afterglow, decreasing markedly with pressure. This is essentially a consequence of the increase in the quenching rates as the pressure increases. Note as well that there is a reduction in the effective electric field in the discharge with pressure [74], which leads to a smaller population of the excited states in the beginning of the afterglow.

5.1.3. Active neutral species. In addition to Ar metastable atoms, Ar–O_2 discharges also contain several active oxygen species that play a crucial role in numerous applications (cf section 1). Figure 7 shows the evolution of the $O_2(X\,^3\Sigma_g^-)$, $O_2(a\,^1\Delta_g)$, $O_2(b\,^1\Sigma_g^+)$, $O(^3P)$ and $O(^1D)$ densities in the afterglow, for different initial gas mixture compositions at 1 mbar.

In the afterglow of a high Ar content discharge, such as 95%Ar, the $O(^3P)$ density stays constant up to about 10 ms when it starts to decrease, while the excited $O(^1D)$ atoms disappear within 0.1 ms, as shown by figure 7(*a*). Concerning the excited molecules, $O_2(a)$ survives longer than 100 ms, while the density of $O_2(b)$ decreases by 2 orders of magnitude within 10 ms of afterglow time. With higher O_2 addition into Ar (from figures 7(*a*)–(*d*)) the depletion of $O(^1D)$ becomes faster, because its volume quenching by O_2 is significantly stronger than by Ar [74], whereas the lifetimes of the other species do not change appreciably. The O_3 density is orders of magnitude lower than that of O_2 molecules, although its density increases strongly with the O_2 percentage in the initial mixture. The evolution of O_3 in the afterglow is shown for the 30%Ar–70%O_2 mixture presented in figure 7(*d*). The ozone can survive for a long time, up to 100 ms, although its density shows a minimum around 1 ms. The increase in the O_3 density in the afterglow after 1 ms occurs due to the decrease in the losses through the $O_2(b) + O_3 \rightarrow O_2(X) + O_2(X) + O(^3P)$ process after the depletion of $O_2(b)$, while the sources due to the $O(^3P)$ assisted processes ($O(^3P) + O_2(X,0) + O \rightarrow O_3 + O$

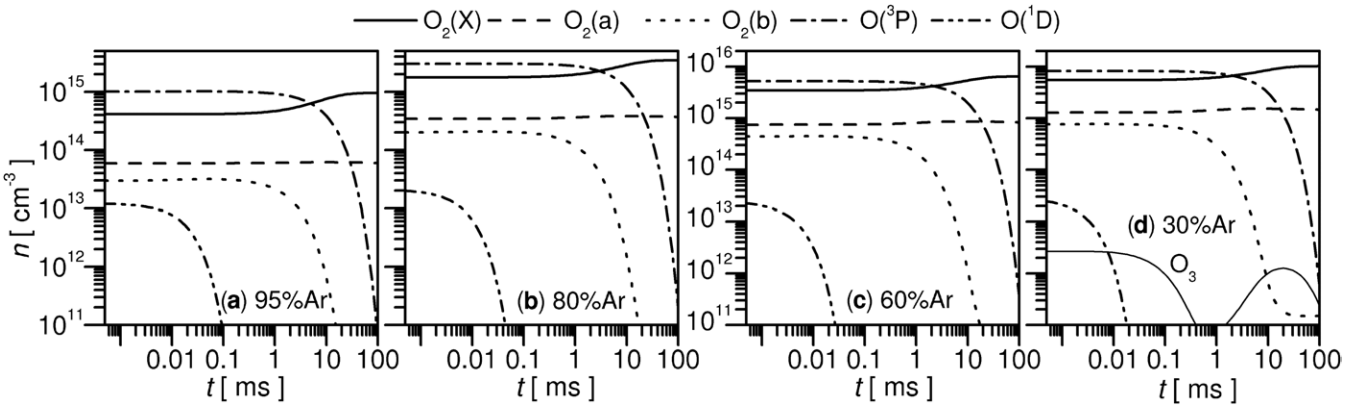

Figure 7. Densities of oxygen species along the early afterglow as a function of the afterglow time, at 1 mbar, for different mixture compositions.

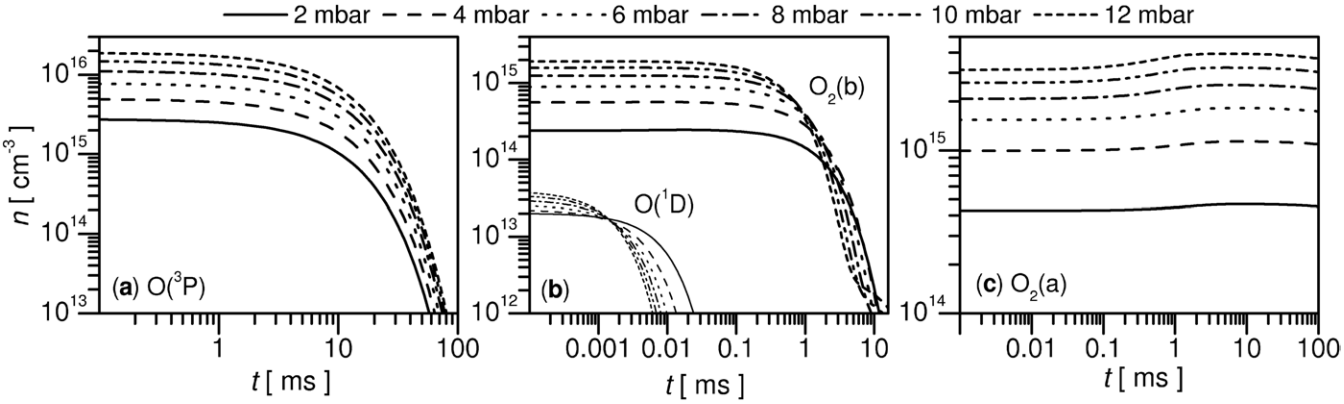

Figure 8. Densities of (*a*) $O(^3P)$, (*b*) $O(^1D)$ and $O_2(b)$, (*c*) $O_2(a)$ along the early afterglow for the 90%Ar–10%O_2 mixture at different gas pressures.

and $O_2 + O_2(X,0) + O(^3P) \rightarrow O_3 + O_2$) keep quasi-constant. The second decrease in the O_3 density, after 10 ms, occurs as a result of the decrease in the sources from the processes mentioned above, following the depletion of the $O(^3P)$ density.

Figures 8(*a*)–(*c*) show the evolution of the oxygen species in the afterglow at different pressures for the 90%Ar–10%O_2 mixture. The lifetime of $O(^3P)$ atoms is relatively independent of the value of the pressure, as it can be seen in figure 8(*a*). With pressure we can observe just a slight increase in the $O(^3P)$ recombination rate. On the other hand, the excited $O(^1D)$ atoms, figure 8(*b*), disappear considerably faster with pressure, although the initial densities are higher at higher pressures. This reflects the fact that $O(^3P)$ atoms are essentially destroyed by wall recombination, while $O(^1D)$ is destroyed by quenching in volume. The $O_2(b)$ concentration starts to decrease slightly earlier in the afterglow when the pressure is increased, figure 8(*b*), since its volume quenching by oxygen atoms is only moderately efficient and wall losses remain expressive [74]. The $O_2(a)$ density profiles, figure 8(*c*), show a slight increase at around 0.1 ms, which becomes more pronounced at higher pressures and is a consequence of the quenching of $O_2(b)$ by oxygen atoms, $O_2(b) + O \rightarrow O_2(a) + O$ [74]. After that they stay quasi-constant up to 100 ms.

One important parameter regarding oxygen atoms, in addition to their absolute densities, is also the dissociation degree, here defined as $[O]/2[O_2]_0$. Figure 9 depicts the absolute $O(^3P)$ concentration and the dissociation degree for different initial gas mixture compositions at 4 mbar, corresponding to one of the preferred pressure values in sterilization and surface treatment experiments [34, 76]. With O_2 addition to Ar the $O(^3P)$ density rises fast in the discharge up to the mixtures with 70%Ar, from where the density increase becomes more moderate, figure 9(*a*). In the afterglow the $O(^3P)$ destruction in different mixtures occurs with a very similar rate, which is due to the fact that $O(^3P)$ is lost predominantly through surface recombination. As a result, within 15 ms in the afterglow a decrease of about a factor of 5 is obtained. A comparison with the experimental data presented in table 1 is also shown, for the 90%Ar–10%O_2 mixture at 10 ms. The calculated $O(^3P)$ density is about 2×10^{15} cm^{-3}, in excellent agreement with the experimental measurements, 1.5×10^{15} cm^{-3} [76] and 1.7×10^{15} cm^{-3} [34], respectively. In what concerns the dissociation degree, contrary to the absolute $O(^3P)$ density, it decreases with the O_2 percentage in the initial mixture composition. In mixtures with 95%Ar dissociation degrees as high as 38% are obtained in the discharge, decreasing to 9% at 15 ms afterglow time. In turn, for a discharge in pure oxygen the dissociation degree is less than 20% and it decreases below 1% within 15 ms in the afterglow.

The pressure dependence of the dissociation degree is investigated in the 90%Ar–10%O_2 mixture for pressure values

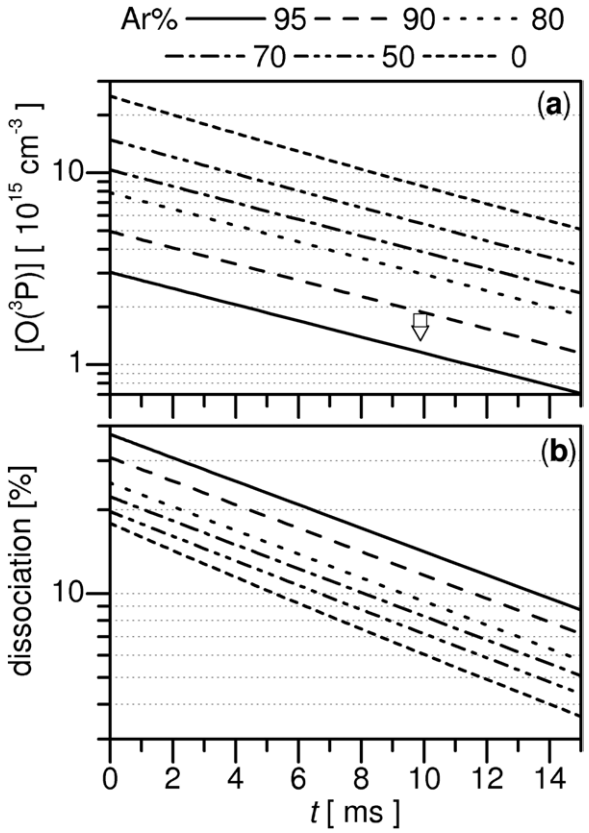

Figure 9. $O(^3P)$ density (*a*) and dissociation degree (*b*) along the early afterglow as a function of the afterglow time, at 4 mbar, for different mixture compositions. The symbols in (*a*) represent the experimental data for the mixture with 90%Ar taken from [76] (▽) and [34] (□).

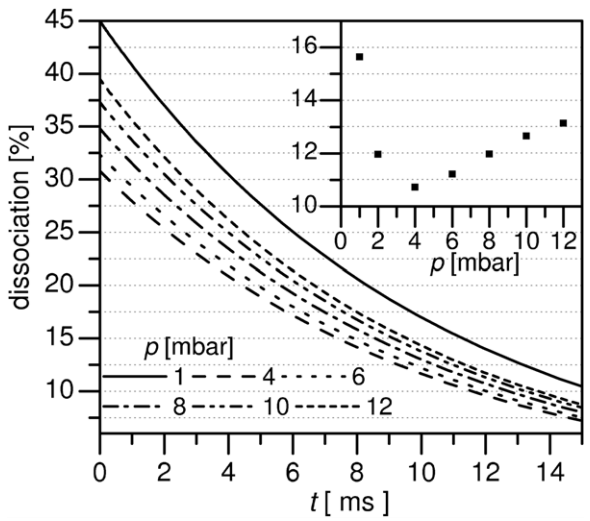

Figure 10. Dissociation degree as a function of the afterglow time in the case of a 90%Ar–10%O_2 initial mixture composition. The inset shows the dissociation degree as a function of pressure at 10 ms afterglow time.

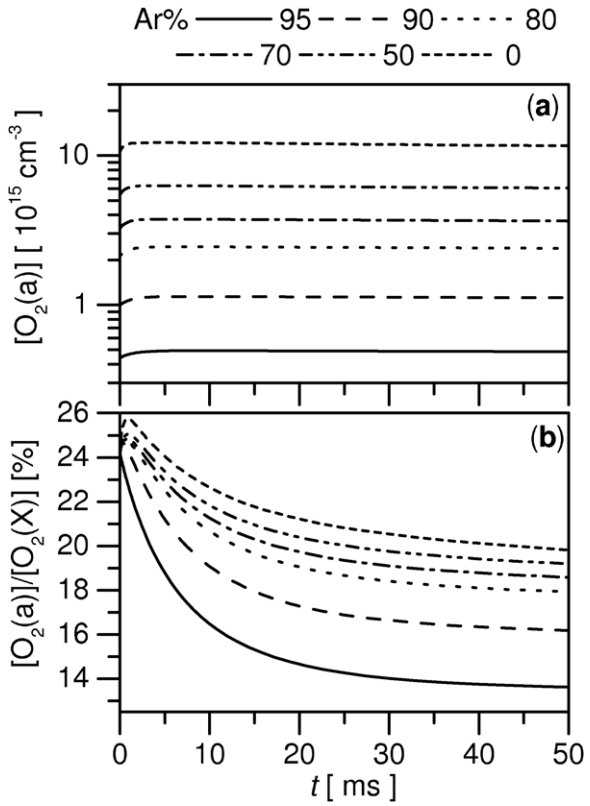

Figure 11. $O_2(a)$ density (*a*) and $O_2(a)$ yield (*b*) along the early afterglow as a function of the afterglow time, at 4 mbar, for different mixture compositions.

in the 1–12 mbar range. Figure 10 shows the dissociation degree as a function of the afterglow time for different pressures. In the domain of pressures investigated here the highest and the lowest dissociation degrees have been obtained at 1 mbar and 4 mbar, respectively, as also illustrated by the inset of figure 10 for 10 ms afterglow time.

The $O_2(a)$ molecules, as discussed in section 1, in addition to their chemical activity, play an important role in the excitation of the oxygen–iodine laser [40, 48–54]. The I^* upper laser state is populated by the $O_2(a)+I \rightarrow O_2(X)+I^*$ process. Due to this excitation mechanism, a population inversion in the iodine atom can take place when the $O_2(a)$ concentration satisfies the condition $[O_2(a)]/[O_2(X)] = Y > (1/2)K_{eq}$, where $[O_2(X)]$ is the concentration of ground-state oxygen molecules, the equilibrium constant $K_{eq} = 0.75\exp(402/T)$ [49] is the ratio of rate constants of forward and backward processes, and Y is the $O_2(a)$ yield. Hence, in order to achieve a positive gain, the yield of $O_2(a)$ should be at least equal to the threshold yield, $Y_{th} = (1/2)K_{eq}$, which at 400 K is 24% [54].

Figure 11 shows the $O_2(a)$ density and yield along the afterglow at 4 mbar for different mixture compositions. This figure reveals that the absolute $O_2(a)$ density increases with O_2 addition to Ar—the density increases by about one order of magnitude when the initial mixture composition is changed from 90%Ar–10%O_2 to pure O_2—and it stays constant in the afterglow for times longer than 50 ms, independently of the mixture composition. On the other hand, the $O_2(a)$ yield decreases in the afterglow after passing through a small maximum at about 1 ms, as can be seen in figure 11(*b*), consistent with the formation of $O_2(a)$ from the quenching of $O_2(b)$ and the concentrations shown in figure 8(*c*). The different behaviours of the $O_2(a)$ density and yield are mostly related to the $O_2(X)$ density, which is correlated with the dissociation degree presented above. In fact, atomic

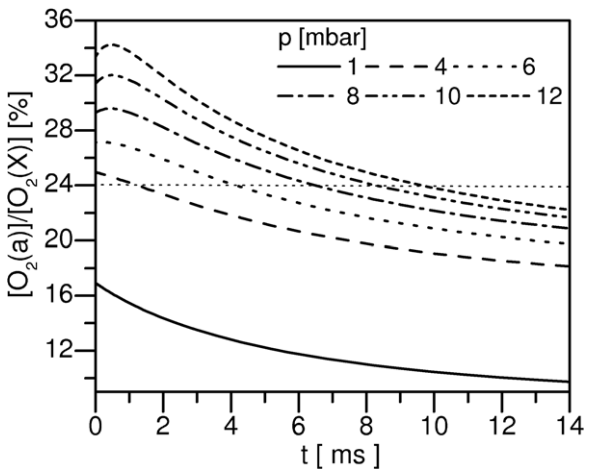

Figure 12. $O_2(a)$ yield as a function of afterglow time at different pressures in the case of 90%Ar–10%O_2 initial mixture composition.

recombination leads to the decrease in the dissociation degree seen in figure 10, with a corresponding increase in the $O_2(X)$ density. In turn, as the the $O_2(a)$ concentration stays approximately constant for long times in the afterglow, the yield decreases. At this pressure, yields slightly higher than the threshold yield can be sustained only up to about 2–5 ms.

Previous investigations have shown that the $O_2(a)$ yield increases with pressure in the 10–100 mbar range [54]. Figure 12 shows the evolution of the yield with pressure for the 90%Ar–10%O_2 case, a mixture that provides a high dissociation degree, for pressures between 1 and 12 mbar. While at 1 mbar the yield at the end of the discharge is much lower than the threshold yield, and at 4 mbar it is just slightly higher than that at 12 mbar, yields as high as 34% are obtained. Moreover, at this pressure, yields above the threshold can be sustained up to 10 ms.

5.2. *Late afterglow*

The late afterglow can be present in a large-volume processing reactor, as the one described in section 3. For several applications it is important to know the three-dimensional distribution of the active species in the whole reactor, as it allows an evaluation of the processing efficiency in different parts of the reactor. The 3D hydrodynamic model presented in section 4 has already been tested in N_2–O_2 systems, where a very good agreement has been obtained between the calculated emitting species density distributions and the corresponding experimentally measured emission intensity distributions [66]. The model is now used to investigate the Ar–O_2 system.

In the late afterglow only the neutral species are followed, since the ions that do not recombine in the early afterglow and manage to enter the reactor will disappear quickly in the reactor in the vicinity of the entrance. Similarly, as shown by the early afterglow results, the Ar metastable and resonant state atoms do not survive long when O_2 is added to Ar. The present 3D calculations confirm that, even if these species would enter the reactor right after the end of the discharge, they would recombine near the entrance. As a consequence, our results will concentrate on the oxygen species density distributions at various discharge conditions, in particular pressure and initial mixture composition, and system configurations, i.e. different positions of the reactor relative to the end of the discharge. In the present calculations the gas flow rate is set to 1000 sccm, while the inlet gas and the wall temperatures are taken to be 500 K and 300 K, respectively.

From the point of view of the applications, the most important species are the $O(^3P)$ atoms and $O_2(a)$ molecules, since the excited $O(^1D)$ atoms recombine very fast in the reactor. As it was shown in figure 8(*a*), the concentration of $O(^3P)$ atoms starts to decrease pronouncedly around 10 ms. Here we investigate two different cases in what concerns the position of the reactor relative to the end of the discharge: (i) $t_{in} = 0$ ms, i.e. the reactor's entrance is positioned right at the end of the discharge column (beginning of the afterglow) and (ii) $t_{in} = 10$ ms. Figure 13 shows the $O(^3P)$ density distribution in the x–z vertical symmetry plane with $y = 15$ cm at different values of pressure and for the two reactor positions, in the case of a 90%Ar–10%O_2 initial mixture composition. At 1 mbar (left column of figure 13) very similar distributions are obtained for the two reactor positions, i.e. the density decreases about one order of magnitude from the entrance—we note that the gas enters the reactor on the left plane ($x = 0$) through the inlet positioned at $z = 14$ cm—to the walls that are not in the flow direction. The $O(^3P)$ density distribution in the reactor at this pressure is mostly influenced by surface recombination (we recall that γ_O on Al is 2×10^{-2}). With increasing pressure the density distribution in the reactor becomes more inhomogeneous. For instance, at 10 mbar and $t_{in} = 0$ (right column of figure 13(*a*)), the density decreases more than one order of magnitude from the entrance to the reactor walls. This reflects the augmentation of the role of volume reactions as the pressure increases. It can also be verified that the differences between the density distributions obtained at $t_{in} = 0$ ms and 10 ms become more pronounced as the pressure increases.

In what concerns the $O_2(a)$ molecules, as shown in figure 8(*c*), the density does not change considerably during the first 100 ms in the afterglow. The 3D calculations conducted in the reactor show that there are no differences between the density distributions obtained for $t_{in} = 0$ ms and 10 ms, respectively. Figure 14 shows the $O_2(a)$ density distribution in the x–z vertical symmetry plane at different pressure values for $t_{in} = 10$ ms in the case of 90%Ar–10%O_2 initial mixture composition. At 1 mbar we can observe the slight increase in the $O_2(a)$ density also shown at around 10 ms by the 0D calculations conducted in the early afterglow tube, see figure 7(*a*). At higher pressures this density increase shifts to lower afterglow times, see figure 8(*c*), therefore it still occurs before the reactor entrance. With increasing pressure, more inhomogeneous density distributions are obtained in the reactor. This results first of all from the decrease in sources due to the $O(^3P) + O(^3P) + O_2 \rightarrow O_2(a) + O_2$ process. The $O(^3P)$ population decreases considerably in the reactor, see figure 13 and consequently increases that of $O_2(X)$. Then it follows an increase in the losses by the $O_2(a) + O_2(X) \rightarrow O_2(X) + O_2(X)$ process.

The calculations conducted in the early afterglow tube have shown that the O_3 density is very low compared with the

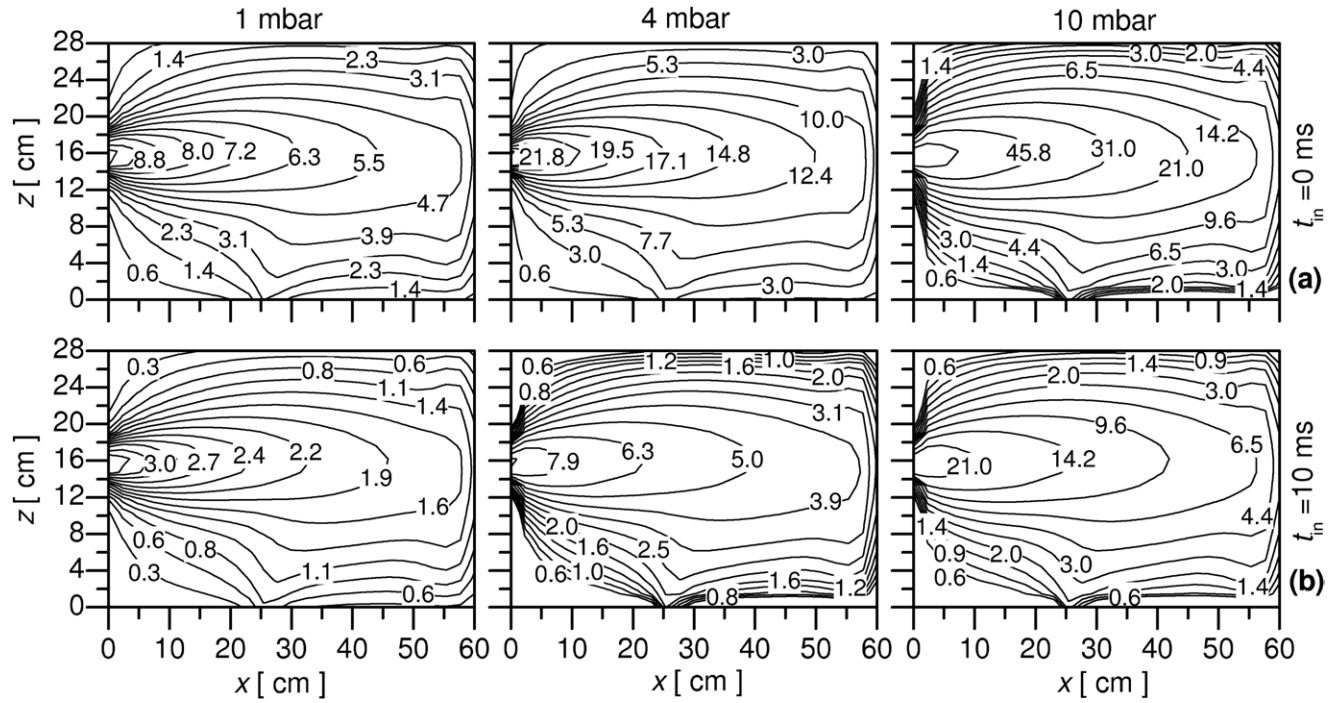

Figure 13. O(^{3}P) density distribution in the x–z vertical symmetry plane with $y = 15$ cm at different pressures for two reactor positions, for a 90%Ar–10%O_2 initial mixture composition. The densities are given in units of 10^{14} cm^{-3}.

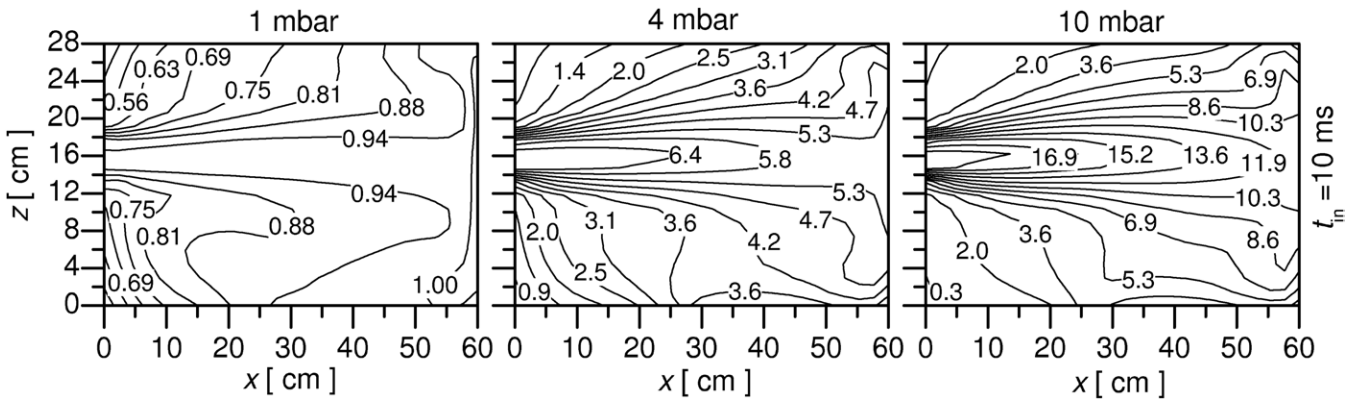

Figure 14. $O_2(a)$ density distribution in the x–z vertical symmetry plane with $y = 15$ cm at different pressures, for a 90%Ar–10%O_2 initial mixture composition. The densities are given in 10^{14} cm^{-3} units.

other oxygen species, although it can slightly increase in the afterglow, while the $O_2(b)$ density drops orders of magnitude between 1 and 10 ms afterglow. Therefore, these species can play a role in the reactor only if the entrance of the reactor is very close to the end of the discharge column. Figure 15 shows the density distributions of $O_2(X)$, $O_2(b)$ and O_3 at 1 mbar, for a 90%Ar–10%O_2 initial mixture composition and in the case $t_{in} = 0$ ms. As already mentioned, the $O_2(X)$ density increases towards the walls due to the O(^{3}P) recombination (first column of figure 15), while the $O_2(b)$ density decreases more than one order of magnitude, mainly due to the strong gas phase quenching processes, but also due to surface losses. In what concerns O_3, the lowest density occurs in the middle of the reactor, the increase in the $O_2(X)$ density towards the walls helping the production of O_3 via the $O_2(X)+O_2(X)+O(^3P) \rightarrow O_3 + O_2(X)$ process.

At a last step we investigate the evolution of the density of the most important oxygen species in the reactor, O(^{3}P) and $O_2(a)$, at different initial mixture compositions. The pressure was set to 1 mbar and three different mixtures were considered: (i) 90%Ar–10%O_2, (ii) 50%Ar–50%O_2 and (iii) 10%Ar–90%O_2. The calculated density distributions are shown in figure 16 for the x–z vertical symmetry plane for $t_{in} = 10$ ms. In the case of O atoms, figure 16(a), similar distributions are obtained for all mixture compositions, i.e. the density decreases about one order of magnitude from the entrance to the top and bottom walls. This also shows that at this pressure the O atom density is governed by the surface reactions. As for the $O_2(a)$ molecules, slightly different distributions are obtained depending on the mixture composition. In the 90%Ar–10%O_2 mixture a small increase in density can be observed in the flow direction, as discussed in previous

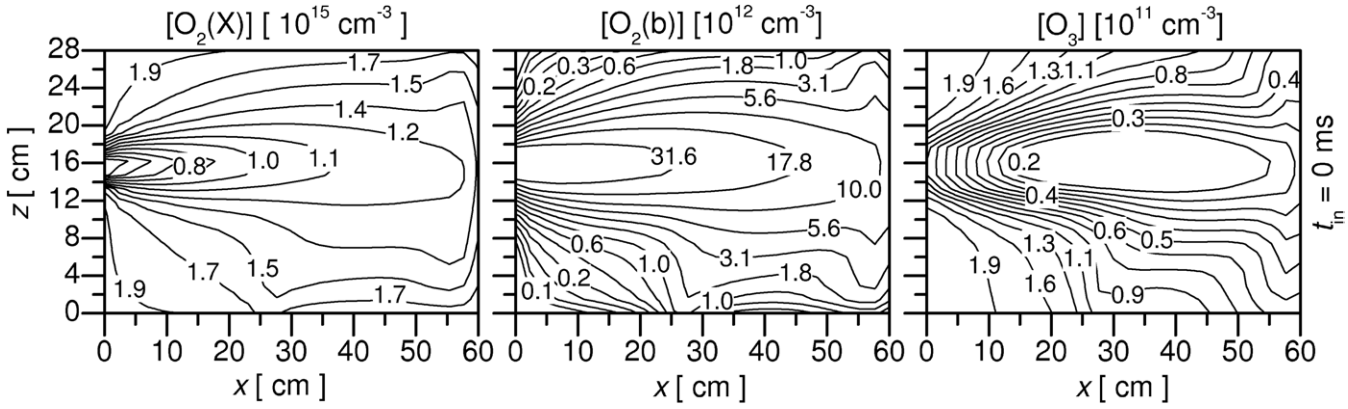

Figure 15. Density distribution of $O_2(X)$, $O_2(b)$ and O_3 in the vertical x–z symmetry plane, for a 90%Ar–10%O_2 initial mixture composition at 1 mbar.

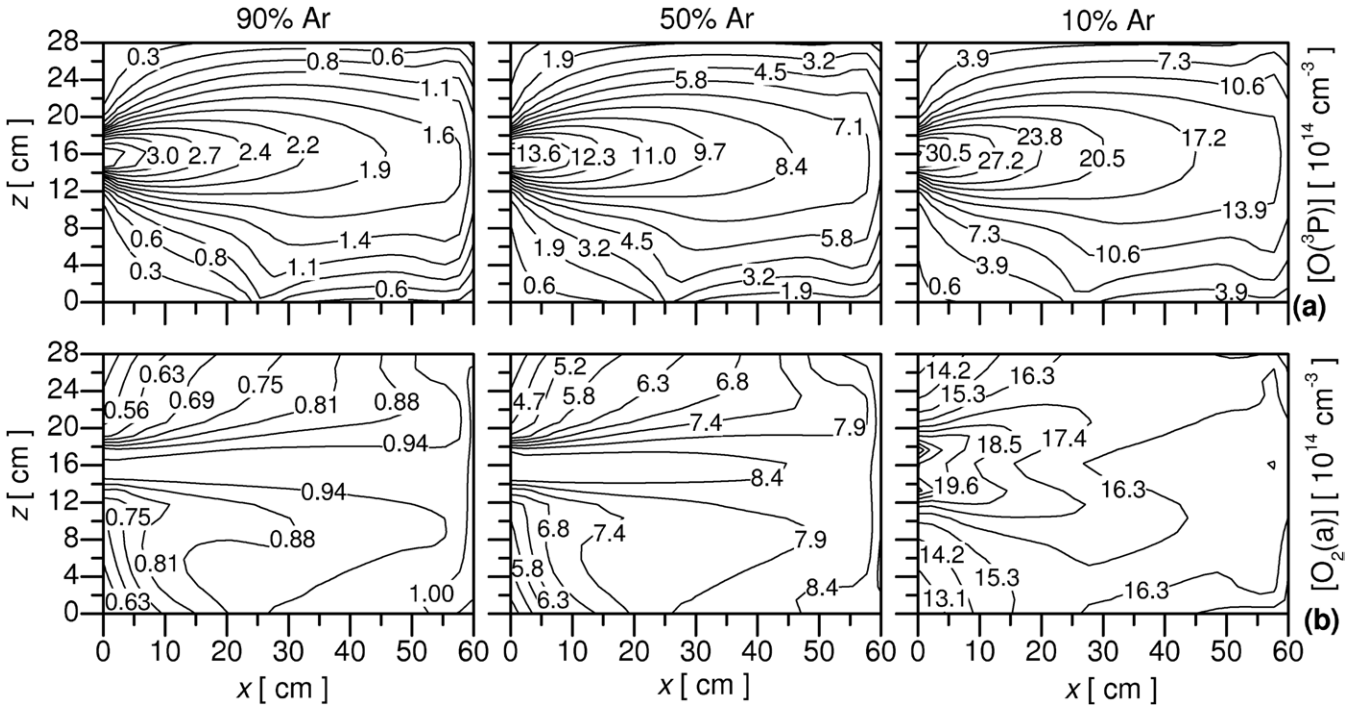

Figure 16. Density distribution of (a) O(^{3}P) and (b)$O_2(a)$ in the vertical x–z symmetry plane for different initial mixture compositions, at 1 mbar and for $t_{in} = 10$ ms.

paragraphs. With 50% O_2 in the mixture the density increase towards the right wall vanishes and the concentration of $O_2(a)$ stays constant along the flow, while for further O_2 addition a density decrease already appears along the flow. At each mixture composition the density decreases from the entrance towards the walls that are not in the flow direction, although the distribution remains quite homogeneous, changing only by about 20%.

As already pointed out, for various applications it is important to determine the O_2 dissociation degree and the yield of $O_2(a)$ molecules, defined as $[O]/2[O_2]_0$ and $[O_2(a)]/[O_2(X)]$, respectively. It is interesting to note that in high O_2 content mixtures, higher than 50%, very similar dissociation degree distributions can be obtained in the reactor, figure 17(a). This could also be predicted from the early afterglow results, cf figure 8. In what concerns the $O_2(a)$ yield, very similar distributions are obtained in the reactor at 1 mbar for each mixture composition, decreasing by about a factor of 3 from the reactor entrance to the walls.

6. Conclusions

In this work we have investigated the flowing afterglow of an Ar–O_2 microwave surface-wave discharge. The system under analysis is composed of a surface-wave discharge generated at pressures between 1 and 12 mbar in a long cylindrical tube of 0.5 cm diameter, an early afterglow developing in a 2.8 cm diameter tube connecting the discharge region with a processing reactor, and a late afterglow taking place in the large-volume 60 cm × 30 cm × 28 cm processing reactor. Similar systems have been used in plasma sterilization experiments [12, 65, 66, 76, 77] and surface treatments [27, 29, 34, 76], the system having further potential in biomedical and nanotechnological applications.

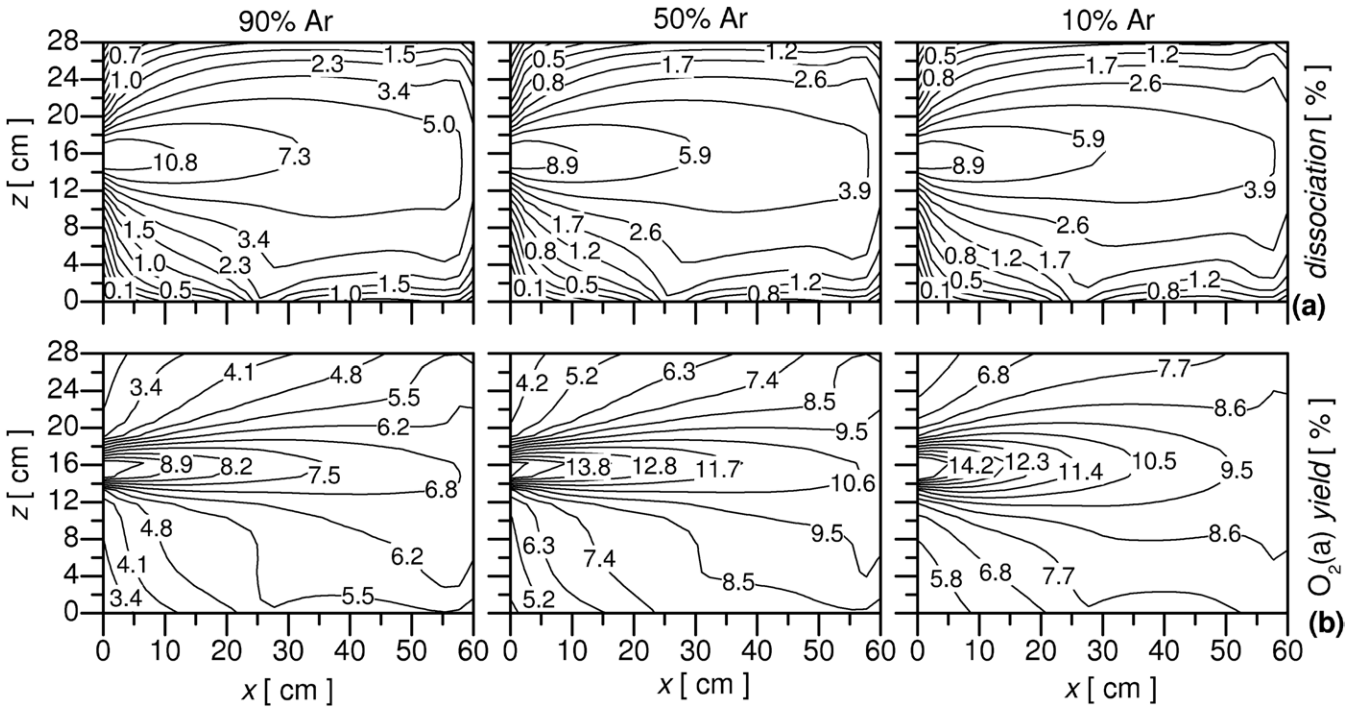

Figure 17. Distribution of (*a*) the dissociation degree and (*b*) $O_2(a)$ yield in the vertical x–z symmetry plane for different initial mixture compositions, at 1 mbar and for $t_{in} = 10$ ms.

To this purpose, we have built a self-consistent kinetic model describing the discharge zone, previously analysed in [74]. The model includes the electron Boltzmann equation and the rate-balance equations describing the creation and destruction of the most important active species, namely $Ar(^1S_0, {}^3P_2, {}^3P_1, {}^3P_0, {}^1P_1)$, $O_2(X\,{}^3\Sigma_g^-, v)$, $O_2(a\,{}^1\Delta_g, b\,{}^1\Sigma_g^+)$, $O(^3P, {}^1D)$, O_3, Ar^+, Ar_2^+, O_2^+, O^+ and O^-. The same system of time-dependent equations is solved in the early afterglow, where the concentrations calculated at the end of the discharge are taken as initial values for the afterglow. The system is solved as a function of 'afterglow time', which can be converted into afterglow position by knowing the gas pressure and flow rate. A smooth transition from the ambipolar to free diffusion regimes is taken into account, in order to evaluate the lifetime of electrons and positive ions in the afterglow. The 3D hydrodynamic model for the late afterglow provides the three-dimensional distribution of the different species in the reactor, by solving the total mass conservation, continuity, total momentum conservation and total energy conservation equations. Systematic calculations have been conducted to study the behaviour of the system with the mixture composition, ranging from pure Ar to pure O_2, and with pressure.

The evolution of the ions in the afterglow was investigated first. It was found that, for discharges in pure argon or with a small oxygen addition, the populations of Ar^+, Ar_2^+, O^+ or O_2^+ may exhibit a maximum in the early afterglow at around 10^{-1} ms. This phenomenon is the result of a combination of different factors. First, there is a transition from ambipolar to free diffusion. When it takes place, the electrons are removed very quickly and the positive ions start to diffuse more slowly. Second, Ar^+ ions are formed by Penning ionization, $Ar(4s_j) + Ar(4s_i) \rightarrow Ar(^1S_0) + Ar^+ + e$. Finally, the other positive ions are created by the charge transfer processes $Ar^+ + Ar(^1S_0) + Ar(^1S_0) \rightarrow Ar_2^+ + Ar(^1S_0)$, $O(^3P) + Ar^+ \rightarrow Ar(^1S_0) + O^+$ and $O(_2) + Ar^+ \rightarrow Ar(^1S_0) + O_2^+$. When the concentration of oxygen in the mixture increases, the phenomenon disappears as the Ar(4s) states responsible for the Penning ionization are strongly quenched by O and O_2. Furthermore, O_2^+ is the dominant ion in the early afterglow for a large number of conditions, its lifetime increasing significantly with pressure, reaching times as long as 10 ms at 12 mbar. This value should be kept in mind when tailoring a system for a particular application, in both cases the presence of ions is desirable and undesirable.

The discharge manifests a high degree of dissociation, which is higher at large argon content in the mixture, and is very effective in creating other active species [74]. Argon metastable and resonant states do not survive long in the early afterglow, their role in late-afterglow conditions being thus questionable. The same is true for $O(^1D)$ excited atoms, which are quenched in volume by molecular oxygen, their lifetime being reduced as the pressure increases. In contrast, oxygen $O(^3P)$ atoms and $O_2(a)$ molecules remain in the afterglow for very long times, so that they can be used in processing. Ground-state $O(^3P)$ atoms can survive up to 10–50 ms, although the dissociation degree decreases to a few per cent at about 10 ms afterglow time. At pressures above 4 mbar a high yield of $O_2(a)$ can be achieved, above the threshold yield for the iodine laser operation [54], which at 12 mbar can be sustained for afterglow times of up to 10 ms.

The late afterglow present in the large-volume reactor was investigated for different gas mixtures, working pressures, and position of the processing reactor in the system. The

dominant species have been found to be O(^{3}P) atoms and O_2(X) and $O_2(a)$ molecules. The calculations have shown that large and rather homogeneous density distributions can be achieved for the active O(^{3}P) and $O_2(a)$ species, especially concerning $O_2(a)$ metastables, which is a desirable result for most applications. A more homogeneous distribution of atomic oxygen can be attained by using other wall materials, corresponding to different recombination probabilities. Work is in progress to quantify this issue.

For the aluminum reactor studied here, at low pressure the density of O(^{3}P) atoms decreases by about one order of magnitude towards the reactor walls, while that of O_2(a) changes by about 20%. However, the density decreases become more pronounced with pressure. Very similar density distributions are found for O(^{3}P) atoms at different mixture compositions. A quasi-homogeneous $O_2(a)$ distribution is found in high Ar content mixtures, which becomes more inhomogeneous with the O_2 addition.

In what concerns the O_2 dissociation degree, its distribution is similar to that of O(^{3}P) atoms, decreasing from about 10% to less than 1% at the walls for any mixture composition. In addition, the $O_2(a)$ yield does not follow the $O_2(a)$ density distribution, since it is also influenced by the O_2(X) concentration. The latter has an increasing distribution towards the walls, due to atomic recombination and the corresponding decrease in the dissociation degree. As a result, the $O_2(a)$ yield distribution in the reactor is more inhomogeneous than the distribution of $O_2(a)$, decreasing about a factor of 2 from the entrance to the walls.

Other species, such as $O_2(b)$, O_3, O(^{1}D) and the VUV emitting Ar(4s) resonant states, have a shorter lifetime and can only pay a relevant role in processing if the reactor is placed close to the end of the discharge. Therefore, applications requiring a strong UV/VUV emission may benefit from the promising ternary Ar–O_2–N_2 mixture, rich in active species and providing NO(A) and NO(B) as additional UV/VUV sources. This mixture will be investigated in the near future.

Acknowledgments

The work has been supported by the Portuguese Fundação para a Ciência e Tecnologia (FCT) funds to Instituto de Plasmas e Fusão Nuclear – Laboratório Associado, the Portuguese FCT through project PTDC/FIS/108411/2009, the Hungarian Science Foundation OTKA through project F-67556 and by Janos Bolyai Research Scholarship of Hungarian Academy of Sciences. The authors want to express their gratitude to Dr Jorge Loureiro for very rewarding discussions.

References

[1] Gudmundsson J T, Kimura T and Lieberman M A 1999 Experimental studies of O_2/Ar plasma in a planar inductive discharge *Plasma Sources Sci. Technol.* **8** 22–30

[2] Gudmundsson J T, Kouznetsov I G, Patel K K and Lieberman M A 2001 Electronegativity of low-pressure high-density oxygen discharges *J. Phys. D: Appl. Phys.* **34** 1100–9

[3] Kitajima T, Nakano T and Makabe T 2006 Increased O(^{1}D) metastable density in highly Ar-diluted oxygen plasmas *Appl. Phys. Lett.* **88** 091501

[4] Gudmundsson J T and Thorsteinsson E G 2007 Oxygen discharges diluted with argon: dissociation processes *Plasma Sources Sci. Technol.* **16** 399–412

[5] Ershov A and Borysow J 2007 Atomic oxygen densities in a downstream microwave O_2/Ar plasma source *Plasma Sources Sci. Technol.* **16** 798–802

[6] Bauville G, Lacour B, Magne L, Puech V, Boeuf J P, Munoz-Serrano E and Pitchford L C 2007 Singlet oxygen production in a microcathode sustained discharge *Appl. Phys. Lett.* **90** 031501

[7] Santos Sousa J, Bauville G, Lacour B, Puech V, Touzeau M and Pitchford L 2008 $O_2(a\,^1\Delta_g)$ production at atmospheric pressure by microdischarge *Appl. Phys. Lett.* **93** 011502

[8] Sato T and Makabe T 2008 A numerical investigation of atomic oxygen density in an inductively coupled plasma in O_2/Ar mixture *J. Phys. D: Appl. Phys.* **41** 035211

[9] Hayashi Y, Hirao S, Zhang Y, Gans T, O'Connell D, Lj Petrović Z and Makabe T 2009 Argon metastable state densities in inductively coupled plasma in mixtures of Ar and O_2 *J. Phys. D: Appl. Phys.* **42** 145206

[10] Soloshenko I A, Tsiolko V V, Khomich V A, Shchedrin A I, Ryabtsev A V, Bazhenov V Y and Mikhno I L 2000 Sterilization of medical products in low-pressure glow discharges *Plasma Phys. Rep.* **26** 792–800

[11] Moreau S, Moisan M, Tabrizian M, Barbeau J, Pelletier J, Ricard A and Yahia L 2000 Using the flowing afterglow of a plasma to inactivate *Bacillus subtilis* spores: Influence of the operating conditions *J. Appl. Phys.* **88** 1166–74

[12] Philip N, Saoudi B, Crevier M C, Moisan M, Barbeau J and Pelletier J 2002 The respective roles of UV photons and oxygen atoms in plasma sterilization at reduced gas pressure: the case of N_2–O_2 mixtures *IEEE IEEE Trans. Plasma Sci.* **30** 1429–36

[13] Villeger S, Cousty S, Ricard A and Sixou M 2003 Sterilization of *E-coli* bacterium in a flowing N_2–O_2 post-discharge reactor *J. Phys. D: Appl. Phys.* **36** L60–2

[14] Nagatsu M, Terashita F, Nonaka H, Xu L, Nagata T and Koide Y 2005 Effects of oxygen radicals in low-pressure surface-wave plasma on sterilization *Appl. Phys. Lett.* **86** 211502

[15] Rossi F, Kylián O and Hasiwa M 2006 Decontamination of surfaces by low pressure plasma discharges *Plasma Process. Polym.* **3** 431–42

[16] Raballand V, Benedikt J, Wunderlich J and von Keudell A 2008 Inactivation of *Bacillus atrophaeus* and of *Aspergillus niger* using beams of argon ions, of oxygen molecules and of oxygen atoms *J. Phys. D: Appl. Phys.* **41** 115207

[17] Vratnica Z, Vujošević D, Cvelbar U and Mozetič M 2008 Degradation of bacteria by weakly ionized highly dissociated radio-frequency oxygen plasma *IEEE Trans. Plasma Sci.* **36** 1300–1

[18] Vicoveanu D, Popescu S, Ohtsu Y and Fujita H 2008 Competing inactivation agents for bacterial spores in radio-frequency oxygen plasmas *Plasma Process. Polym.* **5** 350–8

[19] Cvelbar U, Mozetič M, Hauptman N and Klanjšek-Gunde M 2009 Degradation of *Staphylococcus aureus* bacteria by neutral oxygen atoms *J. Appl. Phys.* **106** 103303

[20] Kylián O, Rauscher H, Gilliland D, Brétagnol F and Rossi F 2008 Removal of model proteins by means of low-pressure inductively coupled plasma discharge *J. Phys. D: Appl. Phys.* **41** 095201

[21] Rossi F, Kylián O, Rauscher H, Hasiwa M and Gilliland D 2009 Low pressure plasma discharges

for the sterilization and decontamination of surfaces *New J. Phys.* **11** 115017

[22] Kylián O and Rossi F 2009 Sterilization and decontamination of medical instruments by low-pressure plasma discharges: application of $Ar/O_2/N_2$ ternary mixture *J. Phys. D: Appl. Phys.* **42** 085207

[23] Rauscher H, Kylián O, Benedikt J, von Keudell A and Rossi F 2010 Elimination of biological contaminations from surfaces by plasma discharges: chemical sputtering *ChemPhysChem* **11** 1382–9

[24] Mozetič M, Cvelbar U, Sunkara M and Vaddiraju S 2005 A method for the rapid synthesis of large quantities of metal oxide nanowires at low temperatures *Adv. Mater.* **17** 2138–42

[25] Cvelbar U, Ostrikov K and Mozetič M 2008 Reactive oxygen plasma-enabled synthesis of nanostructured CdO: tailoring nanostructures through plasma–surface interactions *Nanotechnology* **19** 405605

[26] Yasuda Y, Zaima S, Kaida T and Koide Y 1990 Mechanisms of silicon oxidation at low temperatures by microwave excited O_2 gas and O_2N_2 mixed gas *J. Appl. Phys.* **67** 2603–7

[27] Belmonte T, Czerwiec T, Gavillet J and Michel H 1997 Synthesis of zirconia thin films by RPECVD: modeling of Ar–O_2 post-discharge and comparison between Ar–O_2 and Ar–O_2–H_2 post-discharges processes *Surf. Coat. Technol.* **97** 642–8

[28] Balazs D J, Triandafillu K, Wood P, Chevolot Y, van Delden C, Harms H, Hollenstein C and Mathieu H J 2004 Inhibition of bacterial adhesion on PVC endotracheal tubes by RF-oxygen glow discharge, sodium hydroxide and silver nitrate treatments *Biomaterials* **25** 2139–51

[29] Belmonte T, Pintassilgo C, Czerwiec T, Henrion G, Hody V, Thiebaut J and Loureiro J 2005 Oxygen plasma surface interaction in treatments of polyolefines *Surf. Coat. Technol.* **200** 26–30

[30] Puač N, Petrović Z, Radetić M and Djordjević A 2005 Low pressure RF capacitively coupled plasma reactor for modification of seeds, polymers and textile fabrics *Mater. Sci. Forum* **494** 291–6

[31] Amanatides E, Mataras D, Katsikogianni M and Missirlis Y 2006 Plasma surface treatment of polyethylene terephthalate films for bacterial repellence *Surf. Coat. Technol.* **200** 6331–5

[32] Krstulović N, Labazan I, Milošević S, Cvelbar U, Vesel A and Mozetič M 2006 Optical emission spectroscopy characterization of oxygen plasma during treatment of a PET foil *J. Phys. D: Appl. Phys.* **39** 3799–804

[33] Cvelbar U, Pejovnik S, Mozetič M and Zalar A 2003 Increased surface roughness by oxygen plasma treatment of graphite/polymer composite *Appl. Surf. Sci.* **210** 255–61

[34] Mafra M, Belmonte T, Poncin-Epaillard F, Maliska A and Cvelbar U 2009 Treatment of hexatriacontane by Ar–O_2 remote plasma: formation of the active species *Plasma Process. Polym.* **6** S198–S203

[35] Vesel A, Mozetič M, Hladnik A, Dolenc J, Zule J, Milosevic S, Krstulovic N, Klanjšek-Gunde M and Hauptmann N 2007 Modification of ink-jet paper by oxygen-plasma treatment *J. Phys. D: Appl. Phys.* **40** 3689–96

[36] Klanjšek-Gunde M, Kunaver M, Hrovat A and Cvelbar U 2005 Bonding process efficiency and Al-flake orientation during the curing of powder coatings *Prog. Org. Coat.* **54** 113–9

[37] Mozetic M, Zalar A, Cvelbar U and Babic D 2004 AES characterization of thin oxide films growing on Al foil during oxygen plasma treatment *Surf. Interface Anal.* **36** 986–8

[38] Vesel A, Drenik A, Mozetic M, Zalar A, Balat-Pichelin M and Bele M 2007 AES investigation of the stainless steel surface oxidized in plasma *Vacuum* **82** 228–31

[39] Canal C, Gaboriau F, Ricard A, Mozetic M, Cvelbar U and Drenik A 2007 Density of O-atoms in an afterglow reactor during treatment of wool *Plasma Chem. Plasma Process.* **27** 404–13

[40] Ionin A A, Kochetov I V, Napartovich A P and Yuryshev N N 2007 Physics and engineering of singlet delta oxygen production in low-temperature plasma *J. Phys. D: Appl. Phys.* **40** R25–R61

[41] Midden W R and Wang S Y 1983 Singlet oxygen generation for solution kinetics: clean and simple *J. Am. Chem. Soc.* **105** 4129–35

[42] Tatsuzawa H, Maruyama T, Misawa N, Fujimori K, Hori K, Sano Y, Kambayashi Y and Nakano M 1998 Inactivation of bacterial respiratory chain enzymes by singlet oxygen *FEBS Lett.* **439** 329–33

[43] Ravanat J L, Martinez G R, Medeiros M H, Di Mascio P and Cadet J 2006 Singlet oxygen oxidation of 2′-deoxyguanosine. Formation and mechanistic insights *Tetrahedron* **62** 10709–15

[44] Santos Sousa J, Bauville G, Lacour B, Puech V, Touzeau M and Ravanat J L 2010 DNA oxidation by singlet delta oxygen produced by atmospheric pressure microdischarges *Appl. Phys. Lett.* **97** 141502

[45] Parker J G 1984 The importance of singlet delta oxygen in cancer photoradiation therapy *Johns Hopkins APL Technical Digest* **5** 48–50

[46] Niedre M J, Yu C S, Patterson M S and Wilson B C 2005 Singlet oxygen luminescence as an *in vivo* photodynamic therapy dose metric: validation in normal mouse skin with topical amino-levulinic acid *Br. J. Cancer* **92** 298–304

[47] Rabek J F and Ranby B 1975 Role of singlet oxygen in photo-oxidative degradation and photostabilization of polymers *Polym. Eng. Sci.* **15** 40–43

[48] Carroll D L, Verdeyen J T, King D M, Zimmerman J W, Laystrom J K, Woodard B S, Richardson N, Kittell K, Kushner M J and Solomon W C 2004 Measurement of positive gain on the 1315 nm transition of atomic iodine pumped by $O_2(a\,^1\Delta)$ produced in an electric discharge *Appl. Phys. Lett.* **85** 1320–2

[49] Rawlins W T, Lee S, Kessler W J and Davis S J 2005 Observations of gain on the $I(^2P_{1/2} \rightarrow {}^2P_{3/2})$ transition by energy transfer from $O_2(a\,^1\Delta_g)$ generated by a microwave discharge in a subsonic-flow reactor *Appl. Phys. Lett.* **86** 051105

[50] Woodard B S, Zimmerman J W, Benavides G F, Carroll D L, Verdeyen J T, Palla A D, Field T H, Solomon W C, Davis S J, Rawlins W T and Lee S 2008 Gain and continuous-wave laser oscillation on the 1315 nm atomic iodine transition pumped by an air–helium electric discharge *Appl. Phys. Lett.* **93** 021104

[51] Schmiedberger J, Rohlena K, Jirásek V and Kodymová J 2009 Novel concept of electric discharge oxygen–iodine laser *Eur. Phys. J.* D **54** 239–48

[52] Woodard B S, Zimmerman J W, Benavides G F, Carroll D L, Verdeyen J T, Palla A D, Field T H, Solomon W C, Lee S, Rawlins W T and Davis S J 2010 Demonstration of an iodine laser pumped by an air–helium electric discharge *J. Phys. D: Appl. Phys.* **43** 025208

[53] Hicks A, Bruzzese J R and Adamovich I V 2010 Effect of iodine dissociation in an auxiliary discharge on gain in a pulser-sustainer discharge excited oxygen–iodine laser *J. Phys. D: Appl. Phys.* **43** 025206

[54] Guerra V, Kutasi K and Sá P A 2010 $O_2(a\,^1\Delta_g)$ production in flowing Ar–O_2 surface-wave microwave discharges:

Possible use for oxygen–iodine laser excitation *Appl. Phys. Lett.* **96** 071503
[55] Starik A M, Titova N S, Bezgin L V and Kopchenov V I 2008 Initiation of diffusion combustion in a supersonic flow of H_2–air mixture by electrical-discharge-excited oxygen molecules *J. Phys. D: Appl. Phys.* **41** 125210
[56] Hopf C, Schlüter M and Jacob W 2007 Chemical sputtering of carbon films by argon ions and molecular oxygen at cryogenic temperatures *Appl. Phys. Lett.* **90** 224106
[57] von Keudell A and Jacob W 2004 Elementary processes in plasma-surface interaction: H-atom and ion-induced chemisorption of methyl on hydrocarbon film surfaces *Prog. Surf. Sci.* **76** 21–54
[58] Opretzka J, Benedikt J, Awakowicz P, Wunderlich J and von Keudell A 2007 The role of chemical sputtering during plasma sterilization of *Bacillus atrophaeus J. Phys. D: Appl. Phys.* **40** 2826–30
[59] Munakata N, Hidea K, Kobayashi K, Ito A and Ito T 1986 Action spectra in ultraviolet wavelengths (150–250 nm) for inactivation and mutagenesis of *Bacillus subtilis* spores obtained with synchrotron radiation *Photochem. Photobiol.* **44** 385–90
[60] Halfmann H, Bibinov N, Wunderlich J and Awakowicz P 2007 A double inductively coupled plasma for sterilization of medical devices *J. Phys. D: Appl. Phys.* **40** 4145–54
[61] Halfmann H, Denis B, Bibinov N, Wunderlich J and Awakowicz P 2007 Identification of the most efficient VUV/UV radiation for plasma based inactivation of *Bacillus atrophaeus* spores *J. Phys. D: Appl. Phys.* **40** 5907–11
[62] Pollak J, Moisan M, Kéroack D and Boudam M K 2008 Low-temperature low-damage sterilization based on UV radiation through plasma immersion *J. Phys. D: Appl. Phys.* **41** 135212
[63] Stapelmann K, Kylián O, Denis B and Rossi F 2008 On the application of inductively coupled plasma discharges sustained in $Ar/O_2/N_2$ ternary mixture for sterilization and decontamination of medical instruments *J. Phys. D: Appl. Phys.* **41** 192005
[64] Boudam M K and Moisan M 2010 Synergy effect of heat and UV photons on bacterial-spore inactivation in an N_2–O_2 plasma-afterglow sterilizer *J. Phys. D: Appl. Phys.* **43** 295202
[65] Boudam M K, Saoudi B, Moisan M and Ricard A 2007 Characterization of the flowing afterglows of an N_2–O_2 reduced-pressure discharge: setting the operating conditions to achieve a dominant late afterglow and correlating the NO_β UV intensity variation with the N and O atom densities *J. Phys. D: Appl. Phys.* **40** 1694–711
[66] Kutasi K, Saoudi B, Pintassilgo C D, Loureiro J and Moisan M 2008 Modelling the low-pressure N_2–O_2 plasma afterglow to determine the kinetic mechanisms controlling the UV emission intensity and its spatial distribution for achieving an efficient sterilization process *Plasma Process. Polym.* **5** 840–52
[67] Henriques J, Tatarova E, Dias F M and Ferreira C M 2001 Effect of gas heating on the spatial structure of a travelling wave sustained Ar discharges *J. Appl. Phys.* **90** 4921–8
[68] Henriques J, Tatarova E, Guerra V and Ferreira C M 2002 Wave driven N_2–Ar discharge: I. Self-consistent theoretical model *J. Appl. Phys.* **91** 5622–31
[69] Henriques J, Tatarova E, Dias F M and Ferreira C M 2002 Wave driven N_2–Ar discharge: II. Experiment and comparison with theory *J. Appl. Phys.* **91** 5632–9
[70] de Vries N, Iordanova E, Hartgers A, van Veldhuizen E M, van den Donker M J and van der Mullen J J A M 2006 A spectroscopic method to determine the electron temperature of an argon surface wave sustained plasmas using a collision radiative model *J. Phys. D: Appl. Phys.* **39** 4194–203
[71] Palomares J M, Iordanova E, van Veldhuizen E M, Baede L, Gamero A, Sola A and van der Mullen J J A M 2010 Thomson scattering on argon surfatron plasmas at intermediate pressures: axial profiles of the electron temperature and electron density *Spectrochim. Acta* B **65** 225–33
[72] Pinheiro M J, Gousset G, Granier A and Ferreira C M 1998 Modelling of low-pressure surface wave discharges in flowing oxygen: I. Electrical properties and species concentrations *Plasma Sources Sci. Technol.* **7** 524–36
[73] Pinheiro M J, Gordiets B F and Ferreira C M 1999 Modelling of low-pressure surface wave discharges in flowing oxygen: II. Power dissipation and gas heating *Plasma Sources Sci. Technol.* **8** 31–36
[74] Kutasi K, Guerra V and Sá P 2010 Theoretical insight into Ar–O_2 surface-wave microwave discharges *J. Phys. D: Appl. Phys.* **43** 175201
[75] Ricard A, Gaillard M, Monna V, Vesel A and Mozetič M 2001 Excited species in H_2, N_2, O_2 microwave flowing discharges and post-discharges *Surf. Coat. Technol.* **142–144** 333–6
[76] Ricard A and Monna V 2002 Reactive molecular plasmas *Plasma Sources Sci. Technol.* **11** A150–3
[77] Ricard A, Monna V and Mozetič M 2003 Production of O atoms in Ar–O_2 and N_2–O_2 microwave flowing post-discharges *Surf. Coat. Technol.* **174–175** 905–8
[78] Czerwiec T, Gavillet J, Belmonte T, Michel H and Ricard A 1998 Determination of O atom density in Ar–O_2 and Ar–O_2–H_2 flowing microwave discharges *Surf. Coat. Technol.* **98** 1411–5
[79] Mozetič M, Ricard A, Babič D, Poberaj I, Levaton J, Monna V and Cvelbar U 2003 Comparison of NO titration and fiber optics catalytic probes for determination of neutral oxygen atom concentration in plasmas and postglows *J. Vac. Sci. Technol.* A **21** 369–74
[80] Mozetic M, Vesel A, Cvelbar U and Ricard A 2006 An iron catalytic probe for determination of the O-atom density in an Ar/O_2 afterglow *Plasma Chem. Plasma Process.* **26** 103–17
[81] Mozetič M and Zalar A 2000 Recombination of neutral oxygen atoms on stainless steel surface *Appl. Surf. Sci.* **158** 263–7
[82] Granier A, Pasquiers S, Boisse-Laporte C, Darchicourt R, Leprince P and Marec J 1989 Characterisation of a low-pressure oxygen discharge created by surface waves *J. Phys. D: Appl. Phys.* **22** 1487–96
[83] Margot-Chaker J, Moisan M, Chaker M, Glaude V M M, Lauque P, Paraszczak J and Sauvé G 1989 Tube diameter and wave frequency limitations when using the electro magnetic surface wave in the $m = 1$ (dipolar) mode to sustain a plasma column *J. Appl. Phys.* **66** 4134–48
[84] Allis W P 1956 Motions of ions and electrons *Handbuch der Physik* vol 21 ed S Flügge (Berlin: Springer) pp 383–444
[85] Guerra V, Sá P A and Loureiro J 2001 Relaxation of the electron energy distribution function in the afterglow of a N_2 microwave discharge including space-charge field effects *Phys. Rev.* E **63** 046404
[86] Guerra V, Sá P A and Loureiro J 2004 Kinetic modeling of low-pressure nitrogen discharges and post-discharges *Eur. Phys. J. Appl. Phys.* **28** 125–52
[87] Kutasi K, Pintassilgo C D and Loureiro J 2009 An overview of modelling of low-pressure post-discharge systems used for plasma sterilization *J. Phys.: Conf. Series* **162** 012008
[88] Kutasi K and Loureiro J 2007 Role of the wall reactor material on the species density distributions in an N_2–O_2

post-discharge for plasma sterilization *J. Phys. D: Appl. Phys.* **40** 5612–23
[89] Reid R C and Sherwood T K 1966 *The Properties of Gases and Liquids* 2nd edn (New York: McGraw-Hill)
[90] 1965 *JANAF, Thermochemical Tables* (Midland, MI: Dow Chemical Co.)
[91] Hanley H J M and Ely J F 1973 The viscosity and thermal conductivity coefficients of dilute nitrogen and oxygen *J. Phys. Chem. Ref. Data* **2** 735–56
[92] Hanley H J M, McCarty R D and Haynes W M 1974 The viscosity and thermal conductivity coefficients for dense gaseous and liquid argon, krypton, xenon, nitrogen, and oxygen *J. Phys. Chem. Ref. Data* **3** 979–1017
[93] Younglove B A 1982 Thermophysical properties of fluids: I. Argon, ethylene, parahydrogen, nitrogen, nitrogen trifluoride, and oxygen *J. Phys. Chem. Ref. Data* **11** Suppl. 1, 1–349
[94] Macko P, Veis P and Cernogora G 2004 Study of oxygen atom recombination on a pyrex surface at different wall temperatures by means of time-resolved actinometry in a double pulse discharge technique *Plasma Sources Sci. Technol.* **13** 251–62
[95] Mozetič M 2003 *Thermodynamic Gas Phase* (Ljubljana: DVTS)
[96] Sharpless R L and Slanger T G 1989 Surface chemistry of metastable oxygen: II. Destruction of $O_2(a\,^1\Delta_g)$ *J. Chem. Phys.* **91** 7947–50
[97] Perram G P, Determan D A, Dorian A J, Lowe B F and Thompson T L 1992 Radial diffusion between coaxial cylinders and surface deactivation of $O_2(b\,^1\Sigma_g^+)$ *Chem. Phys.* **162** 427–32
[98] Belmonte T and Noël C 2010 private communication
[99] Kang N, Britun N, Oh S, Gaboriau F and Ricard A 2009 Experimental study of Ar and Ar–N_2 afterglow in a pulse-modulated icp discharge: observation of highly excited Ar(6d) afterpeak emission *J. Phys. D: Appl. Phys.* **42** 112001
[100] Ferreira C M, Loureiro J and Ricard A 1985 Populations in the metastable and the resonance levels of argon and stepwise ionization effects in a low pressure argon positive column *J. Appl. Phys.* **57** 82–90
[101] Sá P A, Loureiro J and Ferreira C M 1992 Effects of electron-electron collisions on the characteristics of dc and microwave discharges in argon at low pressures *J. Phys. D: Appl. Phys.* **25** 960–6